Accepted post-print in *Geochemistry, Geophysics, Geosystems* (DOI: 10.1029/2019GC008219)

How Do Variably Striking Faults Reactivate During Rifting? Insights From Southern Malawi

Jack N. Williams[1*], Åke Fagereng[1]. Luke N. J. Wedmore[2], Juliet Biggs[2], Felix Mphepo[3], Zuze Dulanya[4], Hassan Mdala[3], Thomas Blenkinsop[1]

[1]*School of Earth and Ocean Sciences, Cardiff University, Cardiff, UK*
[2]*School of Earth Sciences, University of Bristol, Bristol, UK*
[3]*Geological Survey Department, Mzuzu Regional Office, Mzuzu, Malawi*
[4]*Geography and Earth Sciences Department, University of Malawi, Zomba, Malawi*

*Corresponding author: J. N. Williams (williamsj132@cardiff.ac.uk)

Key Points

- Proposed stress states for the southern end of the Malawi Rift are tested by assessing fault reactivation potential.
- Variably oriented faults reactivate by all striking slightly obliquely to an ENE-WSW to E-W trending minimum principal compressive stress.
- Faults may locally accommodate pure normal dip slip due to the presence of a deep seated crustal weakness.

Abstract

Crustal extension is commonly thought to be accommodated by faults that strike orthogonal and obliquely to the regional trend of the minimum compressive stress (σ_3). Activation of oblique faults can, however, be conceptually problematic as under Andersonian faulting, it requires preexisting crustal weaknesses, high fluid pressures, and/or stress rotations. Furthermore, measurements of incremental fault displacements, which are typically used to identify oblique faulting, do not necessarily reflect regional stresses. Here, we assess oblique faulting by calculating the stress ratio (σ_3/σ_1, where σ_1 is the maximum compressive stress), slip tendency, and effective coefficient of friction (μ_s') required to reactivate variably striking normal faults under different trends of σ_3. We apply this analysis to NW and NNE striking active faults at the southern end of the Malawi Rift, where NE-SW, ENE-WSW, E-W, and SE-NW σ_3 trends have previously been proposed. A uniform σ_3 trend is inferred for this region as recent joints sets do not rotate along the rift. With a NE-SW trending σ_3, NW-striking faults are well oriented, however, NNE-striking faults require $\mu_s'<0.6$ to reactivate. This is inconsistent with a lack of frictionally weak phyllosilicates detected in the fault zone rocks. With an ENE-WSW to E-W trending σ_3, all faults can reactivate at $\mu_s'>0.55$. These σ_3 trends are also comparable to a focal mechanism stress inversion, regional joint orientations, and previously reported geodetically-derived extension directions. We therefore conclude that unlike typical models of oblique rifting, the southern Malawi Rift consists of faults that all strike slightly oblique to σ_3.

Plain Language Summary

Stretching of the upper brittle part of the Earth's crust should be accommodated by fractures (faults) oriented at 90° to the stretching direction. However, this idealized scenario is rarely observed because of crustal heterogeneities, or because the stretching direction rotates over geological time. Thus, faults are often non-orthogonal (i.e. oblique) to the stretching direction. Here, we use a mechanical analysis to test the obliquity of faults in southern Malawi at the southern juvenile end of the East African Rift system where the crust is actively extending at ~2 mm/year. This section is of interest as fault orientation varies along the rift, and a range of stretching directions have been proposed previously. Our mechanical analysis indicates that extension is most likely accommodated in southern Malawi by faults that are all slightly oblique to an ENE-WSW to E-W stretching direction. This is in contrast to previous models of oblique extension, which suggest that stretching is accommodated by some faults at 90° to the stretching direction, while others are at a very low (<40°) angle to stretching.

Keywords

continental rift, East African Rift, fault reactivation, tectonic stress, normal faults, stress inversions

1. Introduction

Faults in continental rifts often exhibit a wide range of orientations, which can be rationalized in terms of the angle (α) between fault strike and the trend of the minimum principal compressive stress (σ_3). In this context, one set of faults commonly strikes orthogonal to σ_3 (i.e., α~90°), and another set strikes highly obliquely to σ_3 (α<45°). This rifting style has

been proposed for the East African Rift System [EARS; *Corti*, 2012; *Delvaux*, 2001; *Smith & Mosley*, 1993], Rio Grande Rift [*Aldrich*, 1986], Rhine Graben [*Chorowicz & Deffontaines*, 1993; *Lopes Cardozo & Behrmann*, 2006], the Taupō Rift [*Villamor et al.*, 2017], and has been replicated in analog and numerical models [*Acocella et al.*, 1999; *Brune*, 2014; *McClay & White*, 1995; *Withjack & Jamison*, 1986].

There is, however, a fault mechanics problem with the presence of two different sets of fault strikes in continental rifts, as under an Andersonian normal fault stress state and typical rock frictional coefficients [0.6-0.8; *Byerlee*, 1978], α should be consistently ~90°. Oblique fault reactivation therefore requires either preexisting cohesionless [*Etheridge*, 1986; *Morley et al.*, 2004] or frictionally weak planes [*Massironi et al.*, 2011], and/or stress state rotations in time [*Bellahsen et al.*, 2006; *Henstra et al.*, 2015] or space [*Morley*, 2010].

Alternatively, observations of oblique faulting may simply reflect the challenges of determining regional stress directions. Typically, these are inferred from measurements of incremental fault strain (i.e. fault slickensides and earthquake focal mechanisms), which is justified by the prediction that fault slip is parallel to the direction of maximum resolved shear stress on a plane [*Bott*, 1959; *Wallace*, 1951]. However, this "Wallace-Bott criterion" can break down [*Pollard et al.*, 1993; *Twiss & Unruh*, 1998], including cases where rift faults that strike oblique to the regional σ_3 trend accommodate pure normal dip slip [*Corti et al.*, 2013; *Morley*, 2010; *Petit et al.*, 1996; *Philippon et al.*, 2015]. Deriving stress states in rifts from fault slickensides is further complicated because dip slip faults can host oblique slip and even strike slip components due to convergent patterns of coseismic slip [*Hampel et al.*, 2013; *Philippon et al.*, 2015; *Roberts*, 1996]. Therefore, the use of these measurements to infer that a fault is oblique is not necessarily justified.

In this study, we analyze oblique faulting by assuming *a priori* different stress states, and then interpreting their applicability in terms of fault reactivation potential. We use the southern end of the Malawi Rift (Figure 1) as a case example, as geological maps [*Bloomfield & Garson*, 1965; *Habgood et al.*, 1973; *Walshaw*, 1965], fault scarps [*Hodge et al.*, 2018, 2019; *Jackson & Blenkinsop*, 1997; *Wedmore et al.*, 2019], and earthquake focal mechanisms [*Delvaux & Barth*, 2010] demonstrate that active faults switch from NW-SE striking in the Makanjira Graben to NNE-SSW in the Zomba Graben and then back to NW-SE in the Lower Shire Graben as the rift follows an arcuate bend in the high grade metamorphic foliation (Figure 2a). Furthermore, there is an inconsistency in the regional σ_3 trend when inferred from fault slickensides [*Chorowicz & Sorlien*, 1992; *Delvaux et al.*, 2012], fault geometry [*Mortimer et al.*, 2007], earthquake focal mechanisms [*Delvaux & Barth*, 2010], and geodesy [*Stamps et al.*, 2018]. Here, four possible stress states are considered:

- Stress State 1: σ_3 trends SW (06/242, minimum horizonal stress (S_{hmin}) =00/062, Figure 2d), as proposed by an earthquake focal mechanism stress inversion for the Malawi Rift [*Delvaux & Barth*, 2010]. In this way, α is ~90° and ~40° for NW-striking and NNE-striking faults respectively.
- Stress State 2: an ENE-WSW trending σ_3 (10/072, Figure 2e), consistent with individual GPS stations in the Malawi Rift [Figure 1; *Stamps et al.*, 2018] and an updated Malawi rift-wide focal mechanism stress inversion (section 3.2). In this case, α>50° for all faults.
- Stress State 3: an E-W trending σ_3 (00/082, Figure 2f), which is consistent with the extension direction inferred from EARS scale geodetic models [*Stamps et al.*, 2018]

and regional joint orientations (Figure 2c). Thus, both faults sets form slightly oblique to σ_3 (α>60°).

- Stress State 4: stress is spatially heterogenous in southern Malawi, with Proterozoic fabrics actively rotating σ_3 along the rift so that α is consistently ~90° [Figure 2g; *Morley,* 2010].

The reactivation potential of three differently oriented faults in these stress states is then quantified by their stress ratio, slip tendency, and effective coefficient of friction. By comparing these results to the frictional properties of the faults inferred from new field observations and compositional analysis, and deformation experiments performed by *Hellebrekers et al.,* [2019], we can determine which stress state is most applicable in southern Malawi. In doing so, new insights are gained into the applicability of using incremental fault strain measurements in stress inversions, and on the controls on fault geometry in an incipient rift.

2. Geological Setting of the Southern Malawi Rift

The Malawi Rift is a 900-km long section of the EARS Western Branch, and runs from the Rungwe Volcanic Province (RVP) to the Urema Graben (Figures 1 and 2; *Ebinger et al.,* [1987]). It can be divided along its axis into a series of 100- to 150-km long grabens and half grabens with alternating polarities [*Ebinger*, 1989; *Ebinger et al.*, 1987; *Flannery & Rosendahl*, 1990; *Laõ-Dávila et al.*, 2015]. The focus of this study are the three southernmost grabens: the Lower Shire, Zomba, and Makanjira grabens (Figure 2a).

Basement rock within these grabens constitute part of the Southern Irumide Belt (Figure 1), a structurally complex Mesoproterozoic orogenic belt that underwent amphibolite-granulite facies metamorphism during the Pan African orogeny [~800-450 Ma.; *Kröner et al.,* 2001; *Johnson et al.,* 2006; *Fritz et al.,* 2013] . Whether this belt experienced earlier Irumide age deformation (~1020-950 Ma) is unclear [*Andreoli,* 1984; *Fritz et al.*, 2013; *Johnson et al.*, 2006; *Kröner et al.*, 2001; *Manda et al.*, 2019] and the Lower Shire graben may strictly be part of the Neoproterozoic Zambezi Belt [*Chorowicz & Sorlien*, 1992; *Hargrove et al.*, 2003; *Laõ-Dávila et al.*, 2015]. The Lower Shire Graben also underwent NW-SE Karoo extension *[Habgood*, 1963; *Castaing*, 1991], whereas this extension was comparatively minor further north in the Zomba Graben [*Bloomfield*, 1965]. This was followed by a major period of Upper Jurassic-Lower Cretaceous magmatism throughout southern Malawi, which formed the Chilwa Alkaline Province [*Bloomfield*, 1965; *Castaing*, 1991; *Dulanya*, 2017; *Eby et al.*, 1995; *Habgood*, 1963].

$^{40}Ar/^{39}Ar$ dating of the RVP and low temperature thermochronology indicate that the northern part of the Malawi Rift was established by the Oligocene [*Mesko et al.*, 2014; *Mortimer et al.*, 2016; *Roberts et al.*, 2012]; however, there is little chronostratigraphic control on the southern grabens analyzed here [*Dulanya*, 2017]. As elsewhere in the EARS [*Smith & Mosley*, 1993; *Versfelt & Rosendahl*, 1989], these grabens follow the regional moderately dipping foliation (Figure 2a). Thus, a polymodal range [sensu *Healy et al.*, 2015] of NW to NNE striking faults occurs in southern Malawi.

3. Strain and Stress Indicators Within the Malawi Rift

3.1 Previous Estimates of Strain and Stress Within the Malawi Rift

At the scale of the EARS, kinematic models have been developed using a combination of earthquake slip vectors, and continuous and campaign GPS measurements [*Saria et al.*, 2014; *Stamps et al.*, 2008, 2018]. For the Malawi Rift, these models indicate an extension azimuth of 086°±5° relative to a fixed Nubia Plate [*Saria et al.*, 2014; *Stamps et al.*, 2018]. However, the azimuth of individual GPS stations in the rift indicate ENE-WSW extension, except in the vicinity of the RVP [Figure 1; *Stamps et al.*, 2018] .

Delvaux and Barth, [2010] used an earthquake focal mechanism stress inversion to derive a near Andersonian normal fault stress state for the Malawi Rift, with a sub-vertical maximum compressive principal stress (σ_1, 83/070) and sub-horizontal σ_3 (06/242, S_{hmin} =00/062). This S_{hmin} orientation implies NE-SW extension, which is supported by slickenside measurements in the northern part of the Malawi Rift [*Delvaux et al.*, 2012], but differs by 10˚ to 20˚ from the extension directions inferred from geodetic data [*Stamps et al.*, 2018]. Furthermore, this stress inversion predicts that NNE-striking faults accommodate oblique extension (Figure 2d). However, slickensides on these faults indicate nearly pure dip-slip motion and thus approximately NW-SE extension [*Bloomfield & Garson*, 1965; *Chorowicz & Sorlien*, 1992; *Ring et al.*, 1992; *Wedmore et al.*, 2019]. The geometry of faults from seismic reflection surveys within Lake Malawi has also been used to infer NW-SE rift extension [*Mortimer et al.*, 2007; *Scott et al.*, 1992].

3.2 An updated stress inversion for the Malawi Rift

The discrepancy in rift extension direction when inferred from earthquake focal mechanisms, geodetic data, or fault slickensides may reflect the high azimuthal error and limited dataset (13 focal mechanisms across the 900-km long rift) used by *Delvaux and Barth*, [2010]. We therefore performed an inversion with an expanded catalog of 21 focal mechanisms (Table 1 and Figure 1a), which incorporates: (1) the four mainshocks (M_W 5.5-5.9) of the 2009 Karonga earthquake sequence [*Biggs et al.*, 2010; *Gaherty et al.*, 2019; *Hamiel et al.*, 2012], (2) the 2018 M_W 5.5 Nsanje earthquake [*U.S. Department of the Interior U.S. Geological Survey*, 2018], and (3) focal mechanisms from revised bodywave modeling [*Craig et al.*, 2011], which are considered more accurate than the Global Centroid Moment Tensor solutions used in the *Delvaux and Barth*, [*2010*] inversion.

As in *Delvaux and Barth*, [2010], we use Win-Tensor [version 5.8.8, *Delvaux & Sperner*, 2003] to perform the inversion. Here, the data are first processed using the "Right Dihedron Method" to determine the possible range of σ_1 and σ_3 orientations [*Angelier & Mechler*, 1977]. This range is then refined by using "Rotational Optimisation" [*Delvaux & Sperner*, 2003], which seeks to reduce the misfit angle (ω) between the earthquake slip vectors and the azimuth of maximum shear stress within the inversion. This inversion is first run for both nodal planes and then subsequently with just the plane that has the smallest misfit. Focal mechanisms were progressively filtered during the Right Dihedron method analysis using the Counting Deviation method [*Delvaux & Sperner*, 2003, see supporting information Text S1).

The revised stress field shows a 10° clockwise rotation of σ_3 to 10/072 relative to the *Delvaux and Barth*, [2010] inversion (Figure 3). Notably, the new S_{hmin} (00/073) is now consistent with the extension directions from GPS stations in Malawi (Figure 1), and the azimuthal uncertainty has been reduced, from average ω=±21° to ±12°. This may reflect that

Delvaux and Barth, [2010] included all focal mechanisms in their inversion regardless of their compatibility, whereas our increased dataset allowed a more selective approach. However, the uncertainty in this solution is too high (maximum horizonal stress, S_{Hmax}, azimuth one standard deviation uncertainty is ± 22°, Figure 3) to definitively exclude the possibility of E-W or NE-SW extension, or a heterogenous stress state in southern Malawi.

This inversion is also inconsistent with dip slip slickensides on NNE striking faults [*Chorowicz & Sorlien*, 1992; *Wedmore et al.*, 2019]. Stress inversions combining fault slickensides and earthquake focal mechanisms were performed; however, it was not possible to determine a reliable reduced stress tensor as either the data filtering was too severe, or the stress shape ratio ($\Phi=\sigma_2-\sigma_3/\sigma_1-\sigma_3$, where σ_2 is the intermediate principal stress) indicated an unrealistic prolate stress ellipsoid ($\Phi=0.01 \pm 0.04$, *Lisle et al.,* [2006]; Text S1 and Figure S3). Similarly, stress inversions using focal mechanisms from just southern Malawi resulted in stress inversions with $\Phi=0.13 \pm 0.09$ (Figure S4, Text S2). Hence, there is a need to consider other indicators of stress within the rift and fault reactivation potential.

3.3 Joint Orientations

Figures 2 and 4 show the orientations of two steeply-dipping mutually cross-cutting joint sets in southern Malawi, which strike N-S and E-W. Measurements were made in either Southern Irumide Belt basement rocks, which in this region comprise a range of charnockites, metasediments, and mafic paragneisses, or in Upper Jurassic-Late Cretaceous Chilwa Alkaline Province syenites and norites [*Bloomfield*, 1965; *Dawson & Kirkpatrick*, 1968; *Dulanya*, 2017; *Manda et al.*, 2019; *Manyozo et al.*, 1972]. The observation of these joint sets in the latter suggests that they postdate Karoo extension, and a relatively young age is also supported by their open bare surfaces (Figure 4b), which imply formation without any precipitation or annealing processes that could be expected if the joints formed prior to exhumation. Joint orientations were all measured >50 m from faults and are inferred to be outside their respective damage zones.

If it is hypothesized that the N-S striking joints are opening parallel to the trend of σ_3, it is possible to derive another estimate for the σ_3 orientation within southern Malawi. To do this, we quantitatively analyze joint orientations using Kamb Contours (Figure 4a), where contours represent standard deviations away from the expected density of a random sample [*Kamb*, 1959]. This analysis finds that the highest concentration of poles to the N-S striking joint set trends 082°±7°, which is taken here as the joint-derived σ_3 trend. This trend indicates an extension direction that is within error of the extension direction for the Malawi Rift indicated by geodetic models [*Saria et al.*, 2014; *Stamps et al.*, 2018]. The E-W striking joints are interpreted to reflect either an orthogonal joint set to the N-S set, and/or the emplacement of E-W striking Chilwa Akaline Province dykes [*Bloomfield*, 1965]. Many of the N-S striking joints are foliation-parallel and thus may not reflect tectonic stresses [e.g., *Price*, 1959; *Engelder*, 1985; *Williams et al.*, 2018]. However, the N-S striking joint set is also observed within isotropic rocks. Thus, the σ_3 trend (079°±8°, Figure S5) is not significantly changed when foliation-parallel joints are removed from the analysis. This trend is also within error of the revised stress inversion (Figure 3).

4. Fault Strength in Southern Malawi

To calculate fault reactivation potential at the southern end of the Malawi Rift, it is necessary to consider the frictional properties of its faults. We therefore selected three faults (Thyolo,

Chingale Step, and Bilila-Mtakataka, Figure 2a), which (1) encompass the range of fault orientations in southern Malawi, (2) have prominent scarps and are therefore considered active [*Hodge et al.*, 2018, 2019; *Jackson & Blenkinsop*, 1997; *Wedmore et al.*, 2019], and (3) are well exposed, so it is possible to sample them for compositional analysis. The footwall of the Chingale Step and Thyolo faults consist of intensely fractured basement, which is in contact with hanging wall post-Miocene sediments across a <1-m thick fault gouge [Figure 5; *Dulanya*, 2017]. Along most of its length, the Bilila-Mtakataka fault consists of a soil-mantled scarp [*Hodge et al.*, 2018; *Jackson & Blenkinsop*, 1997]. However, at Kasinje (Figure 2a), the fault consists of a 3-m thick unit of fractured gneiss that separates footwall and hanging wall hornblende gneisses [*Hodge et al.*, 2018]

To assess fault zone composition, X-ray diffraction (XRD) analyses were conducted on two samples from each fault: (1) a "country rock" sample from the intact basement closest to the fault, and (2) a "fault rock" sample from the faulted contact itself, that is, the fault gouge for the Thyolo and Chingale Step faults (Figure 5), and fractured gneiss for the Bilila-Mtakataka fault. XRD patterns were collected on powdered samples with a Philips PW1710 Automated Powder Diffractometer using Cu-Kα radiation at 35kV and 40mA, between 2 and 70° 2θ, at a scan speed of 0.04 °2θ/s. From the scans, phases were identified using Philips PC Identify software. Using the peak areas, semi-quantitative analysis was then performed to estimate the weight percentage of each identified phase (Table 2 and Figure S6).

For each fault, we find that the phyllosilicate content is typically <15% (Table 2). This is significant as faults that are frictionally weak (fault static coefficient of friction (μ_s)<0.4) typically contain interconnected phyllosilicates phases that constitute >30%-40% of the fault rock [*Massironi et al.*, 2011; *Moore & Lockner*, 2004]. Thus, we infer that these faults exhibit "Byerlee" frictional strengths (μ_s~0.6-0.8; *Byerlee*, [1978]), which is consistent with the results of deformation experiments on a suite of basement lithologies from the Malawi Rift (μ_s=0.55-0.80; *Hellebrekers et al.*, [2019]). Differences in composition between country rock and fault rock samples are observed, such as for the Chingale Step fault, where calcite is dominant in the fault rock but is not detected in the country rock sample (Table 2). With these samples alone, however, we cannot determine if these differences reflect local protolith variations, near-surface weathering [*Isaacs et al.*, 2007], or fault zone alteration [*Sutherland et al.*, 2012].

5. Fault reactivation potential analysis in southern Malawi

Fault reactivation potential considers how susceptible a fault, of a given orientation and stress state, is to slip under the Mohr-Coulomb failure criterion. This criterion describes the shear stress (τ) required for a fault to exceed its frictional resistance [e.g. *Sibson*, 1985]:

$$\tau = c + \mu_s(\sigma_n - P_f) \quad (1)$$

where σ_n is the normal stress, c is cohesive strength, and P_f is pore fluid pressure. We consider fault reactivation potential in southern Malawi in terms of stress ratio, slip tendency, and effective coefficient of friction (Figure 6).

5.1. Stress ratio

The stress ratio is the ratio between σ_3 and σ_1 required for fault slip [Q=σ_3/σ_1, Figure 6; *Sibson*, 1985]. For the assessed faults, which do not necessarily contain σ_2 in the stress states we consider, we use the 3-D solution outlined by *Leclère and Fabbri*, [2013], where:

$$Q = \frac{-(2AD\mu_s + 2C) \pm \sqrt{\Delta}}{A^2{\mu_s}^2 - C} \quad (2)$$

Here, *A*, *C*, *D* and Δ are functions defined by the stress shape ratio (Φ), *c*, μ_s, magnitude of σ_1, and the direction cosines between the normal to the fault plane and the three principal stress axes (see Text S3).

We calculate *Q* for the three faults described in section 4, given Stress States 1-3 (Figures 2d-2f). For Stress State 1 (NE-SW trending σ_3) we use the principal stress orientations derived in the *Delvaux and Barth*, [2010] stress inversion (σ_1=83/070, σ_2=02/333, σ_3=06/242), for Stress State 2 (ENE-WSW trending σ_3) the orientations derived in the new inversion (σ_1=79/239, σ_2=02/341, σ_3=10/072, Figure 3), and for Stress State 3 (E-W trending σ_3) the orientations based on joint orientations (σ_1=90/000, σ_2=00/172, σ_3=00/082). No reactivation analysis is conducted for the stress rotation hypothesis (Stress State 4, *Morley*, [2010]), as it intrinsically assumes that all faults are favorably oriented for failure (i.e., Figure 6b).

The strike of the Chingale Step and Thyolo faults is constrained from their scarps that are visible in a 12-m resolution TanDEM-X digital elevation model [*Hodge et al.*, 2019; *Wedmore et al.*, 2019]. For the Chingale Step fault, the strike is the orientation of the line that connects the two ends of its scarp, while for the segmented Thyolo fault, strike is the orientation of its longer northwestern section (Figure 2a). Dips of 57° and 60° for the Chingale Step and Thyolo faults were derived from field measurements (Figure 5). The deep structure of the Bilila-Mtakataka fault is best described by two subparallel segments, the longest of which is oriented 156/46 NE [*Hodge et al.*, 2018]. By using these averaged strike measurements, we reduce the influence of fault nonplanarity caused by near-surface topographic stresses on our analysis [*Norris & Cooper*, 1995]. Furthermore, although there is uncertainty in how representative surface measurements of fault dip are, these measurements are similar to those inferred at depth from geophysical surveys and focal mechanisms in the Malawi Rift and elsewhere in the EARS [35-70°, Table 1; *Kolawole et al.*, 2018; *Lavayssière et al.*, 2019; *Mortimer et al.*, 2007; *Wheeler & Rosendahl*, 1994].

As justified in section 4, we infer that these faults exhibit Byerlee frictional strengths, and so μ_s=0.7. A foliation-parallel preexisting fault would generally be considered cohesionless [*Morley et al.*, 2004; *Sibson*, 1985]. However, the high-grade metamorphic fabrics within the Malawi Rift are qualitatively observed to be cohesive (Figure 4b). Furthermore, the rift's geodetically-derived extension rate (~2 mm/yr; *Saria et al.*, [2014]) and EARS Western Branch seismicity b-values [<1; *Hodge et al.*, 2015; *Lavayssière et al.*, 2019] both imply long recurrence intervals between earthquakes, so it is possible that interseismic healing has led to fault cohesion recovery [*Tenthorey & Cox*, 2006]. To account for this ambiguity, we calculate *Q* for end-member cases where *c*=0 and *c*=40 MPa, the latter of which is derived from crystalline rocks typically exhibiting tensile strengths (T_0) of 20 MPa, and that $c \approx 2T_0$ [*Lockner*, 1995; *Sibson*, 1985, 1998].

No knowledge of stress magnitudes is required for calculating *Q* for a cohesionless fault [*Leclère & Fabbri*, 2013]. However, the magnitude of σ_1 is needed to determine *Q* for a cohesive fault, which is calculated by assuming an Andersonian normal fault stress state where:

$$\sigma_1 = \sigma_v = \bar{\rho}(z)gz \quad (3)$$

where σ_v is the vertical stress, g is gravity (9.8 ms^{-2}), z is depth, and $\bar{\rho}(z)$ is the average density of the overlying crust for a given depth, which is a function of an inferred Malawi Rift three-layer crustal model (Table S2; *Nyblade and Langston,* [1995]; *Fagereng,* [2013]). We initially assume the crust is dry, and so the pore fluid pressure, P_f =0; however, the influence of fluids on fault reactivation is discussed in sections 5.3 and 7. The stress shape ratio (Φ) is 0.43, as derived from the updated stress inversion (Figure 3).

5.2 Slip tendency

Slip tendency (T_s) is a measure of the ratio of τ to σ_n acting on the fault surface [*Lisle & Srivastava,* 2004; *Morris et al.*, 1996]:

$$T_s = \frac{\tau}{\sigma_n} \quad (4)$$

For a given stress state, there is a maximum value of T_s, which is that acting on a cohesionless optimally oriented fault [Figure 6; *Lisle & Srivastava,* 2004] . This leads to a normalized index of slip tendency (T'_s) that ranges between 0 and 1:

$$T'_s = \frac{T_s}{\max(T_s)} = \frac{\tau}{\sigma_n tan\phi} \quad (5)$$

(corrected from equation 3 in *Lisle and Srivastava,* [2004]; pers. comm. R. Lisle) where ϕ is the angle of internal fault friction ($\tan\phi=\mu_s$). To calculate T_s and T'_s for the Chingale Step, Thyolo and Bilila-Mtakataka faults without knowledge of the magnitudes of τ and σ_n, we use the solutions outlined by *Lisle and Srivastava,* [2004] (see Text S4). This analysis is performed for Stress States 1-3, assuming μ_s=0.7, P_f=0, and Φ = 0.43.

5.3 Fault effective coefficient of friction

The concept of T_s can be extended to calculate the effective coefficient of friction (μ_s'), which describes the maximum value of μ_s or lowest value of P_f that allows faults to reactivate for a given stress state, without also inducing failure along optimally oriented planes in intact rock [Figure 6; *Sibson,* 1985; *Muluneh et al.,* 2018]. Like T_s, μ_s' is a measure of the ratio of τ to σ_n acting on a fault; however, it is derived using inferred principal stress magnitudes, and fault cohesion can be incorporated. This is advantageous as μ_s' can then be compared to values of μ_s inferred from experimental and compositional analysis of faults to determine if they will reactivate in a given stress state, or if elevated fluid pressures are required.

Principal stress magnitudes can be derived as μ_s' is being equated to the stresses acting on an optimally oriented fault (Figure 6), thus under Mohr-Coulomb theory [*Jaeger et al.*, 2007]:

$$\sigma_1 = 2c\sqrt{\frac{1+\sin\phi_i}{1-\sin\phi_i}} + \sigma_3\left(\frac{1+\sin\phi_i}{1-\sin\phi_i}\right) \quad (6)$$

where $\phi_i=\tan^{-1}\mu_i$, and μ_i is the frictional strength of intact rock. Given the results of *Hellebrekers et al.*, [2019], μ_i =0.7; thus ϕ_i=35°. Since σ_1 can be derived from equation 3, it

is thus also possible to calculate σ_3 and σ_2 by rearranging equation 6 and the equation for Φ (equation S1) respectively. The principal stress magnitudes can then be used to calculate τ and σ_n as a function of depth [*Jaeger et al.*, 2007], and μ_s' can be derived by rearranging the Mohr Coulomb criterion (equation 1). Thus, for the parameters assumed here:

$$\mu_s'(z) = \frac{\sqrt{C\left(\frac{2.7z\bar{\rho}(z)-42}{9.8z\bar{\rho}(z)}\right)^2 - 2C\left(\frac{2.7z\bar{\rho}(z)-42}{9.8z\bar{\rho}(z)}\right) + C} - \frac{c}{\sigma_1}}{A\left(\frac{2.7z\rho(z)-42}{9.8z\bar{\rho}(z)}\right) + B} \quad (7)$$

where the functions *A*, *B*, and *C* are defined by equations S2-S4 (see Text S3 and S5). As previously, we calculate μ_s' for the Thyolo, Chingale Step, and Bilila-Mtakataka faults being reactivated in Stress States 1-3; however, for Stress States 1 and 2, the principal stress axes are slightly rotated so that $\sigma_1=\sigma_v$, and σ_2 and σ_3 equal S_{Hmax} and S_{hmin} respectively. This analysis considers both cohesionless and cohesive faults, and is performed over a depth range of 6-35 km, which encompasses the range of earthquake nucleation in the Malawi Rift [*Biggs et al.*, 2010; *Craig et al.*, 2011; *Nyblade & Langston*, 1995].

The minimum pore fluid pressure (P_f') required to reactivate a fault (Figure 6) can also be calculated as a function of depth, μ_i, and μ_s':

$$P_f'(z) = \sigma_n(z) - \frac{\sigma_n(z)\mu_s'(z)}{\mu_i} \quad (8)$$

(see Text S5). This is calculated with μ_i=0.7 and is plotted in terms of the effective pore-fluid factor ($\lambda_v'=P_f'/\sigma_v$). For comparison, the orientation of the faults is also shown in a stereoplot that is contoured by μ_s' values for each stress state for a given Φ, μ_i, and depth. Plots of the maximum μ_s' that allows all three faults to reactivate for all possible σ_3 trends are also included. As fault reactivation is also influenced by variations in Φ and μ_i [*Boulton et al.*, 2018], we show μ_s' contour plots in Φ-μ_i space for a fixed set of fault and principal stress orientations. In addition, the results of this analysis at a depth of 20 km are shown in 3-D Mohr Space using MohrPlotter v. 2.8.3 [*Allmendinger et al.*, 2011].

6. Fault reactivation potential results

The Thyolo and Bilila-Mtakataka faults have a high reactivation potential under Stress State 1, as their *Q* value is "favorable" and T'_s~1 (Table 3). Thus, they will reactivate under Stress State 1 at relatively high μ_s' (>0.55), regardless of whether they are cohesive or not (Table 3 and Figures 7a, 8a, 9a, S7 and S9). Conversely, the Chingale Step fault is "unfavorably" to "severely misoriented" in this stress state (Table 3), depending on depth and whether it is cohesive. T'_s =0.62, and at depths >10 km, it will not reactivate in Stress State 1 unless μ_s<0.6 or λ_v>0.1 (Table 3 and Figures 8a, 9, S9a, and S10).

In Stress State 3, all faults exhibit T'_s>0.8, although the reactivation potentials of the Thyolo and Bilila-Mtakataka faults are slightly less than under Stress State 1 (Table 3). Therefore, all faults will reactivate at μ_s>0.54 at depths >10 km (Table 3 and Figures 7c, 8c, 9d, and S9c). Fault reactivation potential in Stress State 2 is intermediate between Stress States 1 and 3

except for the Bilila-Mtakataka fault Q and T'_s analysis (Table 3 and Figure 7b, 8b, S9b). This likely reflects the non vertical plunge of σ_1 obtained in this inversion (Figure 3), since intermediate values are observed when σ_1 is assumed to be vertical for the μ_s' calculations. All results for μ_s' are broadly independent of the values of Φ and μ_i (Figures 10 and S11).

7. How do faults in southern Malawi reactivate?

An active fault scarp has been described along Chingale Step fault by *Wedmore et al.*, [2019], and so its orientation is representative of a structure currently accommodating extension. However, if it is cohesionless at 10- to 35-km depth, in Stress State 1 μ_s' is between 0.50 and 0.60 (Figures 9b and S9a). This is at the lower end of frictional strengths inferred from its composition (Table 2) and deformation experiments on basement rocks in Malawi [*Hellebrekers et al.*, 2019]. In the cohesive fault case, μ_s'=0.35-0.45 (Figure 7a, 8a and d), and so below its likely frictional strength.

Alternatively, the Chingale Step fault may reactivate under Stress State 1 at μ_s=0.7 through a moderate increase in fluid pressure (λ_v' 0.1-0.3, Figures 9c and S10), which is sustainable in a normal fault stress state [*Sibson & Rowland*, 2003]. However, post-Miocene hanging wall sediments are <100-m thick in southern Malawi [*Bloomfield & Garson*, 1965; *Mynatt et al.*, 2017; *Walshaw*, 1965], so these faults juxtapose basement rocks across most of the crust. Given that these rocks have been dehydrated during one or more episodes of high grade metamorphism [*Fagereng*, 2013], fluid ingress into these fault zones is likely to be limited [*Hollinsworth et al.*, 2019]. Indeed, even in northern Malawi where sediments are ~500-m thick [*Kolawole et al.*, 2018], there is little fluid involvement in active faulting [*Gaherty et al.*, 2019]. Low fluid pressures around these faults is also illustrated by the lack of extensive vein networks observed in their damage zones [Figure 5; cf *Bruhn et al.*, 1994; *Caine et al.*, 2010; *Sutherland et al.*, 2012].

This reactivation analysis cannot definitively discount stress states; ideally these should be measured using a range of techniques (e.g. borehole breakouts). Nevertheless, it does suggest that previous models of a NW-SE trending σ_3 in Malawi [*Chorowicz & Sorlien*, 1992; *Mortimer et al.*, 2007; *Ring et al.*, 1992] would require unreasonably weak faults (μ_s'<0.5, Figure 8d). Furthermore, it is difficult to account for why a structure with the NNE-SSW strike of the Chingale Step fault would have activated and continue reactivating in Stress State 1, instead of a more optimally oriented fault forming. Conversely, in Stress States 2 and 3, all faults can reactivate at μ_s or P_f that require neither frictionally weak minerals nor elevated fluid pressure (Figures 7-9). In addition, fault slickensides in the Zomba Graben [Figure 5; *Chorowicz & Sorlien*, 1992; *Wedmore et al.*, 2019] indicate NW-SE extension, in contrast to the highly oblique (α<40°) NE-SW extension predicted by applying the Wallace-Bott criterion to Stress State 1. Indeed, it is difficult to reconcile any uniform stress state to the range of NW-SE to NE-SW extension directions that have been proposed for the Malawi Rift based on fault slickensides and earthquake focal mechanisms (see section 3.1).

A range of extension directions could be accounted for by the model proposed in *Morley*, [2010] whereby Southern Irumide metamorphic fabrics rotate σ_3 along the rift, so that all faults are dip slip (i.e., Stress State 4, Figure 2g). In this way, all faults will be favorably oriented for reactivation. Furthermore, although some oblique slip focal mechanisms (Table 1) and fault slickensides are recorded in southern Malawi, in the former case, these tend to be historical focal mechanisms that were not instrumentally well recorded, whilst with regard to

the latter, this may relate to slickensides that record the inherent oblique slip component of normal faulting earthquakes as the fault tip is approached [*Hampel et al.*, 2013; *Philippon et al.*, 2015; *Roberts*, 1996]. There is, however, a discrepancy between Stress State 4 and the homogenous orientation of joint sets in southern Malawi, which suggest a uniform stress state (Figures 2 and 4). The Bilila-Mtakataka and Chingale Step faults also locally cross cut the foliation in a non-systematic manner at the surface [Figure 2a; *Bloomfield,* 1965; *Jackson & Blenkinsop*, 1997 *Hodge et al.*, 2018], further suggesting that the foliation is not actively rotating stresses.

We therefore propose a variation of the *Morley*, [2010] hypothesis that is based on analog models [*Corti et al.*, 2013; *Philippon et al.*, 2015] and which satisfies the constraints of variably striking frictionally strong normal faults, and consistently oriented joints sets. Here, the regional principal stress axes [*sensu Pollard et al.*, 1993] in southern Malawi are uniform but local fault slip vectors [*sensu Twiss and Unruh,* 1998] are rotated to dip slip along the rift by a deep-seated weak ductile shear zone that is oblique to σ_3, but which conditions the kinematics, geometry, and distribution of the rift's faults [*Hodge et al.*, 2018; *Wedmore et al.*, 2019]. Our reactivation analysis indicates that a uniform σ_3 in southern Malawi should trend between ENE-WSW (Stress State 2) and E-W (Stress State 3; Figures 7 and 8). If true, this hypothesis has the following implications:

- A polymodal range of fault orientations at the southern end of the Malawi Rift (Figure 2a) can be accounted for by a uniform stress state and the Mohr Coulomb criterion, given variably oriented pre-existing crustal weaknesses [cf *Healy* et al., 2015].
- NW and NNE striking faults in southern Malawi do not represent a sequential set of highly oblique faults that link faults striking orthogonal to σ_3. Instead, all faults reactivate while striking slightly oblique (α>50°) to a uniformly trending σ_3 (Figures 2e and f).
- Using fault slickensides and earthquake focal mechanisms in stress inversions is problematic as regional stresses and local incremental fault displacements are not necessarily aligned [*Philippon et al.*, 2015; *Twiss & Unruh*, 1998]. Furthermore, accurate principal stress directions will not be derived from stress inversions in which only a subset of fault orientations from a polymodal distribution are included [*Healy et al.*, 2015; *Twiss & Unruh*, 1998].
- This justifies a reassessment of the stress states that have been inferred elsewhere in the Malawi Rift [*Chorowicz & Sorlien*, 1992; *Delvaux & Barth*, 2010; *Mortimer et al.*, 2007; *Ring et al.*, 1992], and other rifts where highly-oblique transfer zones have been proposed [e.g., *Chorowicz & Deffontaines*, 1993; *Acocella et al.*, 1999].
- Normal faults with a wide range of strikes can all reactive within the same stress state, which should be considered when assessing seismic hazard in continental rifts.

8. Conclusions

Previous studies have proposed NE-SW, ENE-WSW, E-W, and SE-NW extension directions in the Malawi Rift. Here, we demonstrate how the reactivation potential of three variably striking active faults supports a σ_3 trend in southern Malawi that lies between ENE-WSW and E-W (Figure 8). Previous estimates of a NW-SE [*Chorowicz & Sorlien*, 1992; *Delvaux*, 2001; *Mortimer et al.*, 2007; *Ring et al.*, 1992] or NE-SW σ_3 trend [*Delvaux et al.*, 2012; *Delvaux & Barth*, 2010] are considered unlikely as they require that some faults in the rift are highly oblique and thus reactivate with unreasonably low frictional strengths and/or high pore

fluid pressures. Furthermore, an ENE-WSW to E-W σ_3 trend is consistent with regional joint sets (Figures 2 and 4), an updated focal mechanism stress inversion (Figure 3), and geodetic data [*Stamps et al.*, 2018]. An alternative hypothesis that foliation actively rotates the stresses along the rift (Stress State 4, Figure 2f; *Morley*, [2010]), is inconsistent with spatially homogeneous joint orientations and local variations in the foliation orientation.

An ENE-WSW to E-W σ_3 trend suggests that all faults in southern Malawi reactivate at slightly oblique angles (angle between fault strike and regional σ_3 trend >50°) and thus counter to typical models of oblique rifting in which one fault set strikes orthogonal to σ_3 and the other is highly oblique [e.g., *Acocella et al.*, 1999; *McClay & White*, 1995]. It is unclear whether this slightly oblique extension is reflected in the kinematics of faults in southern Malawi, or if the faults are actually pure dip slip as indicated by the few well-determined focal mechanisms (Table 1). In the latter case, this can be explained by a deep-seated zone of crustal weakness, which reorients slip [*Corti et al.*, 2013; *Hodge et al.*, 2018; *Philippon et al.*, 2015]. Either way, in rifts where stress states derived from measurements of incremental fault displacement are ambiguous, fault reactivation potential analysis provides a powerful way to test their applicability.

Acknowledgments

This research was funded by the EPSRC Global Challenges Research Fund (grant EP/P028233/1 "PREPARE"). TanDEM-X data were obtained via DLR proposal DEM_GEOL0686. Henri Leclère and Carolyn Boulton are thanked for providing codes to calculate the stress ratio of faults and guidance on how to use them. Antony Oldroyd conducted the XRD analysis and interpretation. We thank Cindy Ebinger and two anonymous reviewers for their constructive comments. All data are included in the main text or supporting information.

References

Acocella, V., Faccenna, C., Funiciello, R., & Rossetti, F. (1999). Sand-box modelling of basement-controlled transfer zones in extensional domains. *Terra Nova*. https://doi.org/10.1046/j.1365-3121.1999.00238.x

Aldrich, M. J. (1986). Tectonics of the Jemez lineament in the Jemez Mountains and Rio Grande Rift (USA). *Journal of Geophysical Research*. https://doi.org/10.1029/JB091iB02p01753

Allmendinger, R. W., Cardozo, N., & Fisher, D. M. (2011). *Structural geology algorithms: Vectors and tensors*. Cambridge University Press.

Andreoli, M. A. G. (1984). Petrochemistry, tectonic evolution and metasomatic mineralisations of Mozambique belt granulites from S Malawi and Tete (Mozambique). *Precambrian Research*, *25*(1–3), 161–186. https://doi.org/10.1016/0301-9268(84)90031-7

Angelier, J., & Mechler, P. (1977). Sur une méthode graphice de recherche des contraintes principales également utilisable en tectonique et en séismologie: La méthode des dièdres droits. *Bulletin de La Société Géologique de France*, *7*(6), 1309–1318. https://doi.org/10.2113/gssgfbull.S7-XIX.6.1309

Bellahsen, N., Fournier, M., D'Acremont, E., Leroy, S., & Daniel, J. M. (2006). Fault reactivation and rift localization: Northeastern Gulf of Aden margin. *Tectonics*. https://doi.org/10.1029/2004TC001626

583 Biggs, J., Nissen, E., Craig, T., Jackson, J., & Robinson, D. P. (2010). Breaking up the
584 hanging wall of a rift-border fault: The 2009 Karonga earthquakes, Malawi. *Geophysical*
585 *Research Letters*, *37*(11). https://doi.org/10.1029/2010GL043179
586 Bloomfield, K. (1958). The geology of the Port Herald Area. *Bulletin of the Geological*
587 *Survey, Malawi*, *9*.
588 Bloomfield, K. (1965). The Geology of the Zomba Area. *Bulletin of the Geological Survey,*
589 *Malawi*, *16*.
590 Bloomfield, K., & Garson, M. S. (1965). The Geology of the Kirk Range-Lisungwe Valley
591 Area. *Bulletin of the Geological Survey, Malawi*, *17*.
592 Bott, M. H. P. (1959). The mechanics of oblique slip faulting. *Geological Magazine*, *96*(2),
593 109–117.
594 Boulton, C., Barth, N. C., Moore, D. E., Lockner, D. A., Townend, J., & Faulkner, D. R.
595 (2018). Frictional properties and 3-D stress analysis of the southern Alpine Fault, New
596 Zealand. *Journal of Structural Geology*, *114*, 43–54.
597 https://doi.org/10.1016/j.jsg.2018.06.003
598 Bruhn, R. L., Parry, W. T., Yonkee, W. a, & Thompson, T. (1994). Fracturing and
599 hydrothermal alteration in normal fault zones. *Pure and Applied Geophysics*, *142*(3),
600 609–644. https://doi.org/10.1007/BF00876057
601 Brune, S. (2014). Evolution of stress and fault patterns in oblique rift systems: 3-D numerical
602 lithospheric-scale experiments from rift to breakup. *Geochemistry, Geophysics,*
603 *Geosystems*, *15*(8), 3392–3415. https://doi.org/10.1002/2014GC005446
604 Byerlee, J. D. (1978). Friction of rocks. *Pure and Applied Geophysics PAGEOPH*, *116*(4–5),
605 615–626. https://doi.org/10.1007/BF00876528
606 Caine, J. S., Bruhn, R. L., & Forster, C. B. (2010). Internal structure, fault rocks, and
607 inferences regarding deformation, fluid flow, and mineralization in the seismogenic
608 Stillwater normal fault, Dixie Valley, Nevada. *Journal of Structural Geology*, *32*(11),
609 1576–1589. https://doi.org/10.1016/j.jsg.2010.03.004
610 Castaing, C. (1991). Post-Pan-African tectonic evolution of South Malawi in relation to the
611 Karroo and recent East African rift systems. *Tectonophysics*, *191*(1–2), 55–73.
612 https://doi.org/10.1016/0040-1951(91)90232-H
613 Chorowicz, J., & Deffontaines, B. (1993). Transfer faults and pull-apart model in the
614 rhinegraben from analysis of multisource data. *Journal of Geophysical Research*.
615 https://doi.org/10.1029/93JB00190
616 Chorowicz, J., & Sorlien, C. (1992). Oblique extensional tectonics in the Malawi Rift, Africa.
617 *Geological Society of America Bulletin*, *104*(8), 1015–1023.
618 https://doi.org/10.1130/0016-7606(1992)104<1015:OETITM>2.3.CO;2
619 Corti, G. (2012). Evolution and characteristics of continental rifting: Analog modeling-
620 inspired view and comparison with examples from the East African Rift System.
621 *Tectonophysics*. https://doi.org/10.1016/j.tecto.2011.06.010
622 Corti, G., Philippon, M., Sani, F., Keir, D., & Kidane, T. (2013). Re-orientation of the
623 extension direction and pure extensional faulting at oblique rift margins: Comparison
624 between the Main Ethiopian Rift and laboratory experiments. *Terra Nova*, *25*(5), 396–
625 404. https://doi.org/10.1111/ter.12049
626 Craig, T. J., Jackson, J. A., Priestley, K., & Mckenzie, D. (2011). Earthquake distribution
627 patterns in Africa: Their relationship to variations in lithospheric and geological
628 structure, and their rheological implications. *Geophysical Journal International*, *185*(1),
629 403–434. https://doi.org/10.1111/j.1365-246X.2011.04950.x
630 Dawson, A. L., & Kirkpatrick, I. M. (1968). The geology of the Cape Maclear peninsula and
631 Lower Bwanje valley. *Bulletin of the Geological Survey, Malawi*, *28*.
632 Delvaux, D. (2001). Tectonic and palaeostress evolution of the Tanganyika-Rukwa-Malawi

rift segment, East African Rift System. *Peri-Tethys Memoir 6: Peri-Tethyan Rift/Wrench Basins and Passive Margins*, 545–567.

Delvaux, D., & Barth, A. (2010). African stress pattern from formal inversion of focal mechanism data. *Tectonophysics*, *482*(1–4), 105–128. https://doi.org/10.1016/j.tecto.2009.05.009

Delvaux, D., & Sperner, B. (2003). New aspects of tectonic stress inversion with reference to the TENSOR program. *Geological Society, London, Special Publications*, *212*(1), 75–100. https://doi.org/10.1144/GSL.SP.2003.212.01.06

Delvaux, D., Kervyn, F., Macheyeki, A. S., & Temu, E. B. (2012). Geodynamic significance of the TRM segment in the East African Rift (W-Tanzania): Active tectonics and paleostress in the Ufipa plateau and Rukwa basin. *Journal of Structural Geology*, *37*, 161–180. https://doi.org/10.1016/j.jsg.2012.01.008

Dulanya, Z. (2017). A review of the geomorphotectonic evolution of the south Malawi rift. *Journal of African Earth Sciences*. https://doi.org/10.1016/j.jafrearsci.2017.02.016

Ebinger, C. J. (1989). Tectonic development of the western branch of the East African rift system. *Geological Society of America Bulletin*. https://doi.org/10.1130/0016-7606(1989)101<0885:TDOTWB>2.3.CO;2

Ebinger, C. J., Rosendahl, B. R., & Reynolds, D. J. (1987). Tectonic model of the Malaŵi rift, Africa. *Tectonophysics*, *141*(1–3), 215–235. https://doi.org/10.1016/0040-1951(87)90187-9

Eby, G. N., Roden-Tice, M., Krueger, H. L., Ewing, W., Faxon, E. H., & Woolley, A. R. (1995). Geochronology and cooling history of the northern part of the Chilwa Alkaline Province, Malawi. *Journal of African Earth Sciences*, *20*(3–4), 275–288. https://doi.org/10.1016/0899-5362(95)00054-W

Engelder, T. (1985). Loading paths to joint propagation during a tectonic cycle: an example from the Appalachian Plateau, U.S.A. *Journal of Structural Geology*, *7*(3–4), 459–476. https://doi.org/10.1016/0191-8141(85)90049-5

Etheridge, M. A. (1986). On the reactivation of extensional fault systems. *Philosophical Transactions - Royal Society of London, Series A*. https://doi.org/10.1098/rsta.1986.0031

Fagereng, Å. (2013). Fault segmentation, deep rift earthquakes and crustal rheology: Insights from the 2009 Karonga sequence and seismicity in the Rukwa-Malawi rift zone. *Tectonophysics*, *601*, 216–225. https://doi.org/10.1016/j.tecto.2013.05.012

Flannery, J. W., & Rosendahl, B. R. (1990). The seismic stratigraphy of Lake Malawi, Africa: implications for interpreting geological processes in lacustrine rifts. *Journal of African Earth Sciences*, *10*(3), 519–548. https://doi.org/10.1016/0899-5362(90)90104-M

Fritz, H., Abdelsalam, M., Ali, K. A., Bingen, B., Collins, A. S., Fowler, A. R., et al. (2013). Orogen styles in the East African Orogen: A review of the Neoproterozoic to Cambrian tectonic evolution. *Journal of African Earth Sciences*. https://doi.org/10.1016/j.jafrearsci.2013.06.004

Gaherty, J. B., Zheng, W., Shillington, D. J., Pritchard, M. E., Henderson, S. T., Chindandali, P. R. N., et al. (2019). Faulting processes during early-stage rifting: Seismic and geodetic analysis of the 2009-2010 Northern Malawi earthquake sequence. *Geophysical Journal International*, *217*(3), 1767–1782. https://doi.org/10.1093/gji/ggz119

Habgood, F. (1963). The geology of the country west of the Shire River between Chikwawa and Chiromo. *Bulletin of the Geological Survey, Malawi*, *14*.

Habgood, F., Holt, D. N., & Walshaw, R. D. (1973). The geology of the Thyolo Area. *Bulletin of the Geological Survey, Malawi*, *22*.

Hamiel, Y., Baer, G., Kalindekafe, L., Dombola, K., & Chindandali, P. (2012). Seismic and aseismic slip evolution and deformation associated with the 2009-2010 northern Malawi earthquake swarm, East African Rift. *Geophysical Journal International*, *191*(3), 898–

908. https://doi.org/10.1111/j.1365-246X.2012.05673.x

Hampel, A., Li, T., & Maniatis, G. (2013). Contrasting strike-slip motions on thrust and normal faults: Implications for space-geodetic monitoring of surface deformation. *Geology*, *41*(3), 299–302. https://doi.org/10.1130/G33927.1

Hargrove, U. S., Hanson, R. E., Martin, M. W., Blenkinsop, T. G., Bowring, S. A., Walker, N., & Munyanyiwa, H. (2003). Tectonic evolution of the Zambezi orogenic belt: Geochronological, structural, and petrological constraints from northern Zimbabwe. *Precambrian Research*. https://doi.org/10.1016/S0301-9268(03)00066-4

Healy, D., Blenkinsop, T. G., Timms, N. E., Meredith, P. G., Mitchell, T. M., & Cooke, M. L. (2015). Polymodal faulting: Time for a new angle on shear failure. *Journal of Structural Geology*. https://doi.org/10.1016/j.jsg.2015.08.013

Hellebrekers, N., Niemeijer, A., Fagereng, Å., Manda, B., & Mvula, R. (2019). Lower crustal earthquakes in the East African Rift System: Insights from frictional properties of rock samples from the Malawi Rift. *EarthArXiv*. https://doi.org/10.31223/osf.io/nu7rq

Henstra, G. A., Rotevatn, A., Gawthorpe, R. L., & Ravnås, R. (2015). Evolution of a major segmented normal fault during multiphase rifting: The origin of plan-view zigzag geometry. *Journal of Structural Geology*, *74*, 45–63. https://doi.org/10.1016/j.jsg.2015.02.005

Hodge, M., Biggs, J., Goda, K., & Aspinall, W. (2015). Assessing infrequent large earthquakes using geomorphology and geodesy: the Malawi Rift. *Natural Hazards*, *76*(3), 1781–1806. https://doi.org/10.1007/s11069-014-1572-y

Hodge, M., Fagereng, A., Biggs, J., & Mdala, H. (2018). Controls on Early-Rift Geometry: New Perspectives From the Bilila-Mtakataka Fault, Malawi. *Geophysical Research Letters*, *45*(9), 3896–3905. https://doi.org/10.1029/2018GL077343

Hodge, M., Biggs, J., Fagereng, A., Elliott, A., Mdala, H., & Mphepo, F. (2019). A semi-automated algorithm to quantify scarp morphology (SPARTA): Application to normal faults in southern Malawi. *Solid Earth*, *10*(1), 27–57. https://doi.org/10.5194/se-10-27-2019

Hollinsworth, A. D., Koehn, D., Dempster, T. J., & Aanyu, K. (2019). Structural controls on the interaction between basin fluids and a rift flank fault: Constraints from the Bwamba Fault, East African Rift. *Journal of Structural Geology*, *118*, 236–249. https://doi.org/10.1016/j.jsg.2018.10.012

Isaacs, A. J., Evans, J. P., Song, S.-R., & Kolesar, P. T. (2007). Structural, Mineralogical, and Geochemical Characterization of the Chelungpu Thrust Fault, Taiwan. *Terrestrial, Atmospheric and Oceanic Sciences*, *18*(2), 183. https://doi.org/10.3319/TAO.2007.18.2.183(TCDP)

Jackson, J., & Blenkinsop, T. (1997). The Bilila-Mtakataka fault in Malawi: an active, 100-km long, normal fault segment in thick seismogenic crust. *Tectonics*, *16*(1), 137–150. https://doi.org/10.1029/96TC02494

Jaeger, J. C., Cook, N. G., & Zimmerman, R. (2007). *Fundamentals of Rock Mechanics, 4th edition*. Wiley-Blackwell.

Johnson, S. P., De Waele, B., & Liyungu, K. A. (2006). U-Pb sensitive high-resolution ion microprobe (SHRIMP) zircon geochronology of granitoid rocks in eastern Zambia: Terrane subdivision of the Mesoproterozoic Southern Irumide Belt. *Tectonics*, *25*(6). https://doi.org/10.1029/2006TC001977

Kamb, W. B. (1959). Ice petrofabric observations from Blue Glacier, Washington, in relation to theory and experiment. *Journal of Geophysical Research*, *64*(11), 1891. https://doi.org/10.1029/JZ064i011p01891

Kolawole, F., Atekwana, E. A., Laó-Dávila, D. A., Abdelsalam, M. G., Chindandali, P. R., Salima, J., & Kalindekafe, L. (2018). Active Deformation of Malawi Rift's North Basin

Hinge Zone Modulated by Reactivation of Preexisting Precambrian Shear Zone Fabric. *Tectonics*, *37*(3), 683–704. https://doi.org/10.1002/2017TC004628

Kröner, A., Willner, A. P., Hegner, E., Jaeckel, P., & Nemchin, A. (2001). Single zircon ages, PT evolution and Nd isotopic systematics of high-grade gneisses in southern Malawi and their bearing on the evolution of the Mozambique belt in southeastern Africa. *Precambrian Research*, *109*(3–4), 257–291. https://doi.org/10.1016/S0301-9268(01)00150-4

Laõ-Dávila, D. A., Al-Salmi, H. S., Abdelsalam, M. G., & Atekwana, E. A. (2015). Hierarchical segmentation of the Malawi Rift: The influence of inherited lithospheric heterogeneity and kinematics in the evolution of continental rifts. *Tectonics*, *34*(12), 2399–2417. https://doi.org/10.1002/2015TC003953

Lavayssière, A., Drooff, C., Ebinger, C., Gallacher, R., Illsley-Kemp, F., Oliva, S. J., & Keir, D. (2019). Depth Extent and Kinematics of Faulting in the Southern Tanganyika Rift, Africa. *Tectonics*, *38*(0). https://doi.org/10.1029/2018TC005379

Leclère, H., & Fabbri, O. (2013). A new three-dimensional method of fault reactivation analysis. *Journal of Structural Geology*, *48*, 153–161. https://doi.org/10.1016/j.jsg.2012.11.004

Lisle, R. J., & Srivastava, D. C. (2004). Test of the frictional reactivation theory for faults and validity of fault-slip analysis. *Geology*. https://doi.org/10.1130/G20408.1

Lisle, R. J., Orife, T. O., Arlegui, L., Liesa, C., & Srivastava, D. C. (2006). Favoured states of palaeostress in the Earth's crust: evidence from fault-slip data. *Journal of Structural Geology*, *28*(6), 1051–1066. https://doi.org/10.1016/j.jsg.2006.03.012

Lockner, D. A. (1995). Rock failure. *Rock Physics and Phase Relations: A Handbook of Physical Constants*, *3*, 127–147.

Lopes Cardozo, G. G. O., & Behrmann, J. H. (2006). Kinematic analysis of the Upper Rhine Graben boundary fault system. *Journal of Structural Geology*. https://doi.org/10.1016/j.jsg.2006.03.010

Manda, B. W. C., Cawood, P. A., Spencer, C. J., Prave, T., Robinson, R., & Roberts, N. M. W. (2019). Evolution of the Mozambique Belt in Malawi constrained by granitoid U-Pb, Sm-Nd and Lu-Hf isotopic data. *Gondwana Research*, *68*, 93–107. https://doi.org/10.1016/j.gr.2018.11.004

Manyozo, D. M., Mandla, A. T., & Phiri, F. R. (1972). The Geology of the Lake Malombe area. *Bulletin of the Geological Survey, Malawi*, *33*.

Massironi, M., Bistacchi, A., & Menegon, L. (2011). Misoriented faults in exhumed metamorphic complexes: Rule or exception? *Earth and Planetary Science Letters*, *307*(1–2), 233–239. https://doi.org/10.1016/j.epsl.2011.04.041

McClay, K. R., & White, M. J. (1995). Analogue modelling of orthogonal and oblique rifting. *Marine and Petroleum Geology*. https://doi.org/10.1016/0264-8172(95)92835-K

Mesko, G. T., Class, C., Maqway, M. D., Boniface, N., Manya, S., & Hemming, S. R. (2014). The timing of early magmatism and extension in the southern East African rift: Tracking geochemical source variability with 40Ar/39Ar geochronology at the Rungwe Volcanic Province, SW Tanzania. In *AGU Fall Meeting Abstracts*.

Moore, D. E., & Lockner, D. a. (2004). Crystallographic controls on the frictional behavior of dry and water-saturated sheet structure minerals. *Journal of Geophysical Research*, *109*(B03401), 1–16. https://doi.org/10.1029/2003JB002582

Morley, C. K. (2010). Stress re-orientation along zones of weak fabrics in rifts: An explanation for pure extension in "oblique" rift segments? *Earth and Planetary Science Letters*, *297*(3–4), 667–673. https://doi.org/10.1016/j.epsl.2010.07.022

Morley, C. K., Haranya, C., Phoosongsee, W., Pongwapee, S., Kornsawan, A., & Wonganan, N. (2004). Activation of rift oblique and rift parallel pre-existing fabrics during

783 extension and their effect on deformation style: Examples from the rifts of Thailand.
784 *Journal of Structural Geology*, *26*(10), 1803–1829.
785 https://doi.org/10.1016/j.jsg.2004.02.014
786 Morris, A., Ferrill, D. A., & Henderson, D. B. (1996). Slip-tendency analysis and fault
787 reactivation. *Geology*. https://doi.org/10.1130/0091-
788 7613(1996)024<0275:STAAFR>2.3.CO;2
789 Mortimer, E. J., Paton, D. A., Scholz, C. A., Strecker, M. R., & Blisniuk, P. (2007).
790 Orthogonal to oblique rifting: Effect of rift basin orientation in the evolution of the
791 North basin, Malawi Rift, East Africa. *Basin Research*, *19*(3), 393–407.
792 https://doi.org/10.1111/j.1365-2117.2007.00332.x
793 Mortimer, E. J., Kirstein, L. A., Stuart, F. M., & Strecker, M. R. (2016). Spatio-temporal
794 trends in normal-fault segmentation recorded by low-temperature thermochronology:
795 Livingstone fault scarp, Malawi Rift, East African Rift System. *Earth and Planetary*
796 *Science Letters*, *455*, 62–72. https://doi.org/10.1016/j.epsl.2016.08.040
797 Muluneh, A. A., Kidane, T., Corti, G., & Keir, D. (2018). Constraints on fault and crustal
798 strength of the Main Ethiopian Rift from formal inversion of earthquake focal
799 mechanism data. *Tectonophysics*, *731–732*, 172–180.
800 https://doi.org/10.1016/j.tecto.2018.03.010
801 Mynatt, W. G., Beresh, S. C. M., Elifritz, E. A., Johnson, S., Mendez, K., Mayle, M., et al.
802 (2017). Imaging of the Subsurface Expression of the Bilila-Mtakataka Fault Using
803 Electrical Resistivity in the Central Malawi Rift. In *AGU Fall Meeting Abstracts*.
804 Norris, R. J., & Cooper, A. F. (1995). Origin of small-scale segmentation and transpressional
805 thrusting along the Alpine Fault, New Zealand. *Geological Society of America Bulletin*,
806 *107*(2), 231–240. https://doi.org/10.1130/0016-
807 7606(1995)107<0231:OOSSSA>2.3.CO;2
808 Nyblade, A. A., & Langston, C. A. (1995). East African earthquakes below 20 km depth and
809 their implications for crustal structure. *Geophysical Journal International*, *121*(1), 49–
810 62. https://doi.org/10.1111/j.1365-246X.1995.tb03510.x
811 Petit, C., Déverchère, J., Houdry, F., Sankov, V. A., Melnikova, V. I., & Delvaux, D. (1996).
812 Present-day stress field changes along the Baikal rift and tectonic implications.
813 *Tectonics*, *15*(6), 1171–1191. https://doi.org/10.1029/96TC00624
814 Philippon, M., Willingshofer, E., Sokoutis, D., Corti, G., Sani, F., Bonini, M., & Cloetingh,
815 S. (2015). Slip re-orientation in oblique rifts. *Geology*, *43*(2), 147–150.
816 https://doi.org/10.1130/G36208.1
817 Pollard, D. D., Saltzer, S. D., & Rubin, A. M. (1993). Stress inversion methods: are they
818 based on faulty assumptions? *Journal of Structural Geology*.
819 https://doi.org/10.1016/0191-8141(93)90176-B
820 Price, N. J. (1959). Mechanics of jointing in rocks. *Geological Magazine*, *96*(2), 149–167.
821 https://doi.org/10.1017/S0016756800060040
822 Ring, U., Betzler, C., & Delvaux, D. (1992). Normal vs. strike-slip faulting during rift
823 development in East Africa: The Malawi rift. *Geology*, *20*(11), 1015–1018.
824 https://doi.org/10.1130/0091-7613(1992)020<1015:NVSSFD>2.3.CO;2
825 Roberts, E. M., Stevens, N. J., O'Connor, P. M., Dirks, P. H. G. M., Gottfried, M. D., Clyde,
826 W. C., et al. (2012). Initiation of the western branch of the East African Rift coeval with
827 the eastern branch. *Nature Geoscience*, *5*(4), 289–294. https://doi.org/10.1038/ngeo1432
828 Roberts, G. P. (1996). Variation in fault-slip directions along active and segmented normal
829 fault systems. *Journal of Structural Geology*, *18*(6), 835–845.
830 https://doi.org/10.1016/S0191-8141(96)80016-2
831 Sandwell, D., Mellors, R., Tong, X., Wei, M., & Wessel, P. (2011). Open radar
832 interferometry software for mapping surface Deformation. *Eos, Transactions American*

Geophysical Union. https://doi.org/10.1029/2011EO280002

Saria, E., Calais, E., Stamps, D. S., Delvaux, D., & Hartnady, C. J. H. (2014). Present-day kinematics of the East African Rift. *Journal of Geophysical Research: Solid Earth*, *119*(4), 3584–3600. https://doi.org/10.1002/2013JB010901

Scott, D. L., Etheridge, M. A., & Rosendahl, B. R. (1992). Oblique-slip deformation in extensional terrains: A case study of the lakes Tanganyika and Malawi Rift Zones. *Tectonics*, *11*(5), 998–1009. https://doi.org/10.1029/92TC00821

Sibson, R. H. (1985). A note on fault reactivation. *Journal of Structural Geology*, *7*(6), 751–754. https://doi.org/10.1016/0191-8141(85)90150-6

Sibson, R. H. (1998). Brittle failure mode plots for compressional and extensional tectonic regimes. *Journal of Structural Geology*, *20*(5), 655–660. https://doi.org/10.1016/S0191-8141(98)00116-3

Sibson, R. H., & Rowland, J. V. (2003). Stress, fluid pressure and structural permeability in seismogenic crust, North Island, New Zealand. *Geophysical Journal International*, *154*(2), 584–594. https://doi.org/10.1046/j.1365-246X.2003.01965.x

Smith, M., & Mosley, P. (1993). Crustal heterogeneity and basement influence on the development of the Kenya Rift, East Africa. *Tectonics*, *12*(2), 591–606. https://doi.org/10.1029/92TC01710

Stamps, D. S., Calais, E., Saria, E., Hartnady, C., Nocquet, J. M., Ebinger, C. J., & Fernandes, R. M. (2008). A kinematic model for the East African Rift. *Geophysical Research Letters*, *35*(5). https://doi.org/10.1029/2007GL032781

Stamps, D. S., Saria, E., & Kreemer, C. (2018). A Geodetic Strain Rate Model for the East African Rift System. *Scientific Reports*. https://doi.org/10.1038/s41598-017-19097-w

Sutherland, R., Toy, V. G., Townend, J., Cox, S. C., Eccles, J. D., Faulkner, D. R., et al. (2012). Drilling reveals fluid control on architecture and rupture of the Alpine fault, New Zealand. *Geology*, *40*(12), 1143–1146. https://doi.org/10.1130/G33614.1

Tenthorey, E., & Cox, S. F. (2006). Cohesive strengthening of fault zones during the interseismic period: An experimental study. *Journal of Geophysical Research: Solid Earth*, *111*(9). https://doi.org/10.1029/2005JB004122

Twiss, R. J., & Unruh, J. R. (1998). Analysis of fault slip inversions: Do they constrain stress or strain rate? *Journal of Geophysical Research: Solid Earth*, *103*(B6), 12205–12222. https://doi.org/10.1029/98jb00612

U.S. Department of the Interior U.S. Geological Survey. (2018). M 5.5 - 24km NE of Nsanje, Malawi [available at https://earthquake.usgs.gov/earthquakes/eventpage/us1000d1cy#executive, last accessed 26 Sept 2018].

Versfelt, J., & Rosendahl, B. R. (1989). Relationships between pre-rift structure and rift architecture in Lakes Tanganyika and Malawi, East Africa. *Nature*. https://doi.org/10.1038/337354a0

Villamor, P., Nicol, A., Seebeck, H., Rowland, J., Townsend, D., Massiot, C., et al. (2017). Tectonic structure and permeability in the Taupô Rift: new insights from analysis of LiDAR derived DEMs. In *Proceedings 39th New Zealand Geothermal Workshop* (Vol. 22, p. 24).

Wallace, R. E. (1951). Geometry of shearing stress and relation to faulting. *The Journal of Geology*, *59*(2), 118–130.

Walshaw, R. D. (1965). The Geology of the Nchue-Balaka Area. *Bulletin of the Geological Survey, Malawi*, *19*.

Wedmore, L., Biggs, J., Williams, J. N., Fagereng, Å., Dulanya, Z., Mphepo, F., & Mdala, H. (2019). Distributed active fault scarps in southern Malawi and the implications for the evolution of strain in amagmatic continental rifts. *EarthArXiv*.

https://doi.org/10.31223/osf.io/ujchx

Wheeler, W. H., & Rosendahl, B. R. (1994). Geometry of the Livingstone Mountains Border Fault, Nyasa (Malawi) Rift, East Africa. *Tectonics*, *13*(2), 303–312. https://doi.org/10.1029/93TC02314

Williams, J. N., Toy, V. G., Massiot, C., McNamara, D. D., Smith, S. A. F., & Mills, S. (2018). Controls on fault zone structure and brittle fracturing in the foliated hanging wall of the Alpine Fault. *Solid Earth*, *9*(2), 469–489. https://doi.org/10.5194/se-9-469-2018

Withjack, M. O., & Jamison, W. R. (1986). Deformation produced by oblique rifting. *Tectonophysics*, *126*(2–4), 99–124. https://doi.org/10.1016/0040-1951(86)90222-2

List of figures

Figure 1

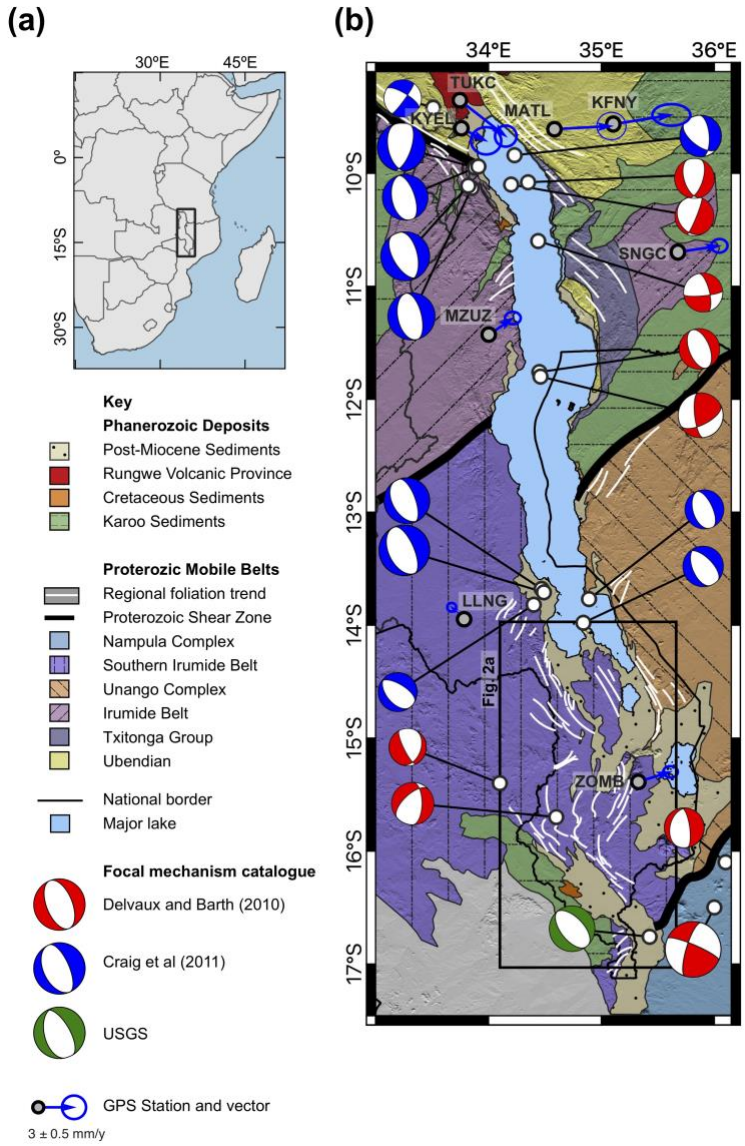

Figure 1: (a) Location of the Malawi Rift within East Africa. (b) Simplified geological map of the rift with Proterozoic units after *Fritz et al.*, [2013], and underlain by Shuttle Radar Topography Mission 30-m digital elevation model [*Sandwell et al.*, 2011]. Location of focal mechanisms listed in Table 1 and vectors from GPS stations for a fixed Nubia Plate reference frame reported by *Stamps et al.*, [2018] also given. Foliation trends collated from SRTM images, field measurements and previous studies [*Bloomfield*, 1958, 1965; *Bloomfield & Garson*, 1965; *Habgood et al.*, 1973; *Hodge et al.*, 2018].

905 Figure 2

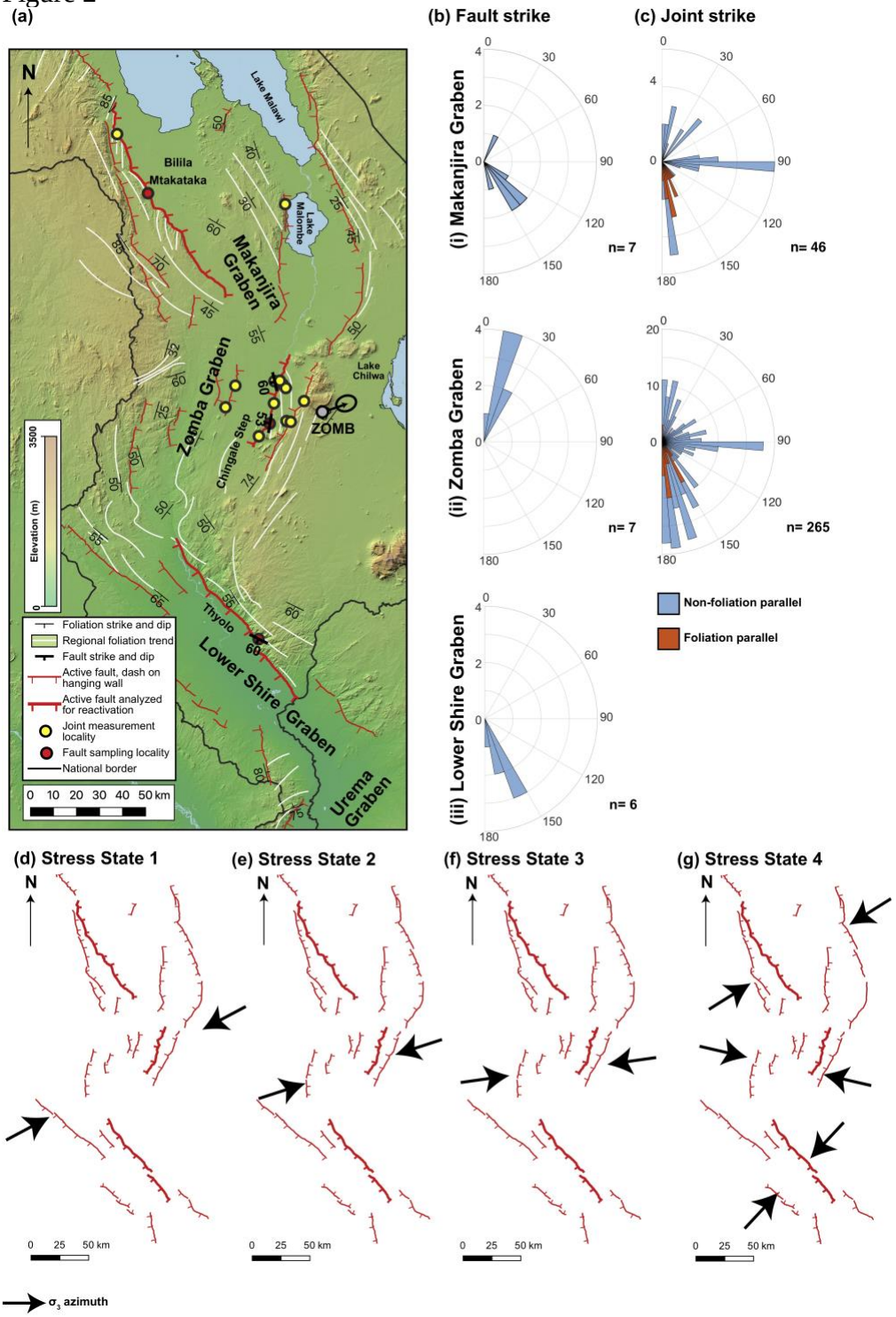

906

907 Figure 2: (a) Map of active faults in southern Malawi collated from TanDEM-X digital elevation
908 model and geological maps [*Bloomfield*, 1958, 1965; *Bloomfield & Garson*, 1965; *Habgood et al.*,
909 1973; *Hodge et al.*, 2018, 2019; *Walshaw*, 1965; *Wedmore et al.*, 2019]. Area shown is indicated in
910 Figure 1b. The azimuth of the ZOMB GPS station [*Stamps et al.*, 2018], and joint and fault field
911 localities are also shown. Rose plots for measurements of (b) fault and (c) joint strike for each of the
912 grabens. (d-g) Schematic representation of the minimum horizontal stress (S_{hmin}) azimuth in Stress
913 States 1-4 with respect to faults in southern Malawi. Area shown for each map is the same as in (a).
914 Weighted fault lines are those in which reactivation analysis was conducted.

915 Figure 3

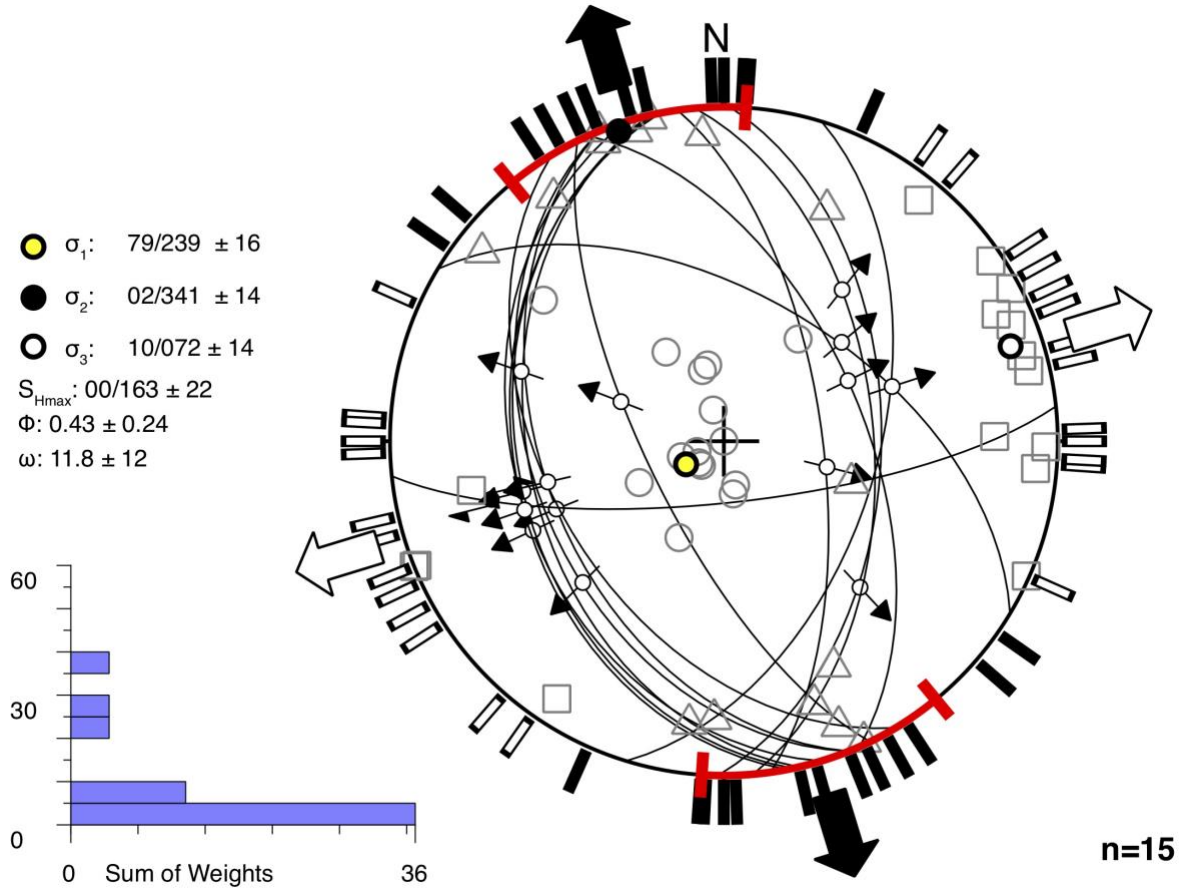

916
917 Figure 3: Results of earthquake focal mechanism stress inversion for the Malawi Rift using
918 Win-Tensor [*Delvaux & Sperner*, 2003] and the mechanisms listed in Table 1. Lower-
919 hemisphere equal area stereoplot depicts selected nodal planes (black lines) with slip vectors
920 (black arrows), the three principal stress axes, maximum and minimum horizontal stress
921 (S_{Hmax} and S_{hmin}) trajectories (black and white arrows outside stereoplot respectively), 1
922 standard deviation error bars for S_{Hmax} (red arc), S_{Hmax} and S_{hmin} trajectories for individual
923 focal mechanisms (black and white bars outside stereoplot), and kinematic axes for individual
924 focal mechanisms (grey circle: *p* axis, triangle: *b* axis, square: *t* axis). Histogram represents
925 distribution of misfit angles (ω), weighted arithmetically according to magnitude. One
926 standard deviation of each parameter is also reported.

927

928 Figure 4

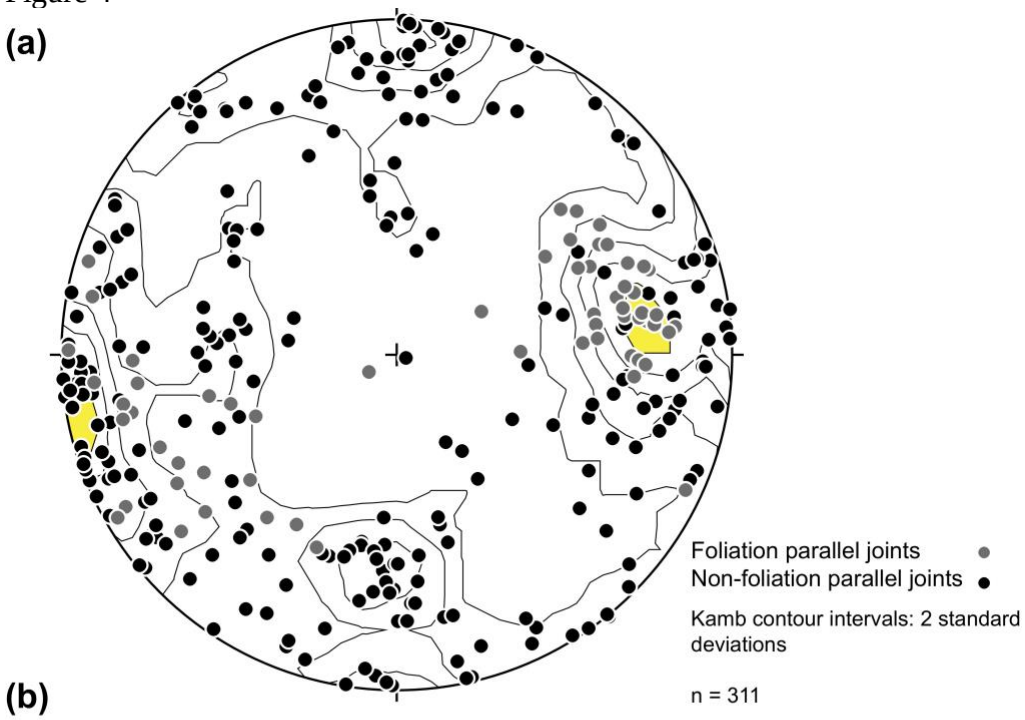

929
930 Figure 4: (a) Stereoplot showing poles to joint orientations that are also shown in Figure 2c.
931 Shaded contour interval indicates highest concentration of the N-S striking joints. The trend
932 at the centre of this interval (082°) is used to infer the trend of the minimum principal stress
933 (σ_3) for Stress State 2. The range of this interval is ±7°. (b) Examples of joint sets in the
934 Malawi Rift. The joint set the facing the photo is a steeply dipping N-S set, which are
935 mutually cross cutting with an inclined E-W set.

936 Figure 5

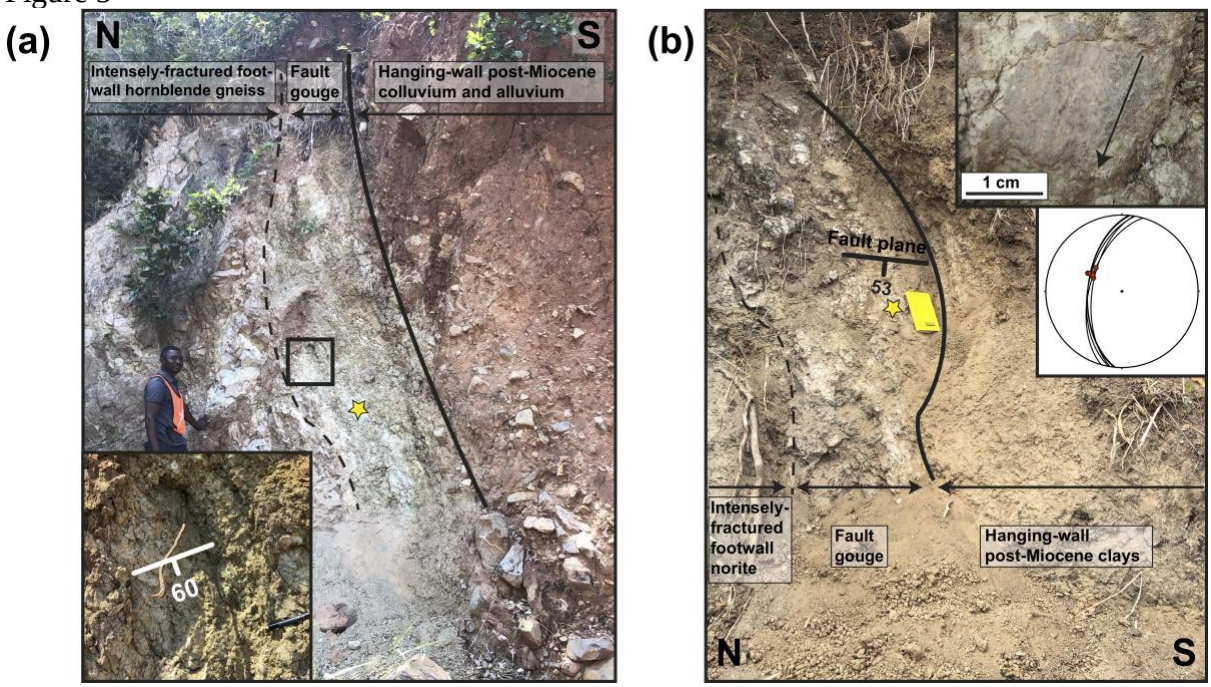

937

938 Figure 5: Examples of outcrops from the (a) Thyolo and (b) Chingale Step faults. Stars depict
939 where "fault rock" samples were taken from for these faults. Footwall and hanging wall unit
940 descriptions taken from *Habgood et al.,* [1973] and *Bloomfield,* [1965] respectively. Box in
941 (a) highlights plane that was used to measure dip of Thyolo fault and is shown in the inset.
942 Inset in (b) shows fault slickensides and orientations plotted on a lower hemisphere equal
943 area stereonet [*Wedmore et al.*, 2019]. Note that a dip of 57° was used for the Chingale Step
944 fault reactivation analysis, based on the average dip measured over other sites (Figure 2a).

945

946 Figure 6

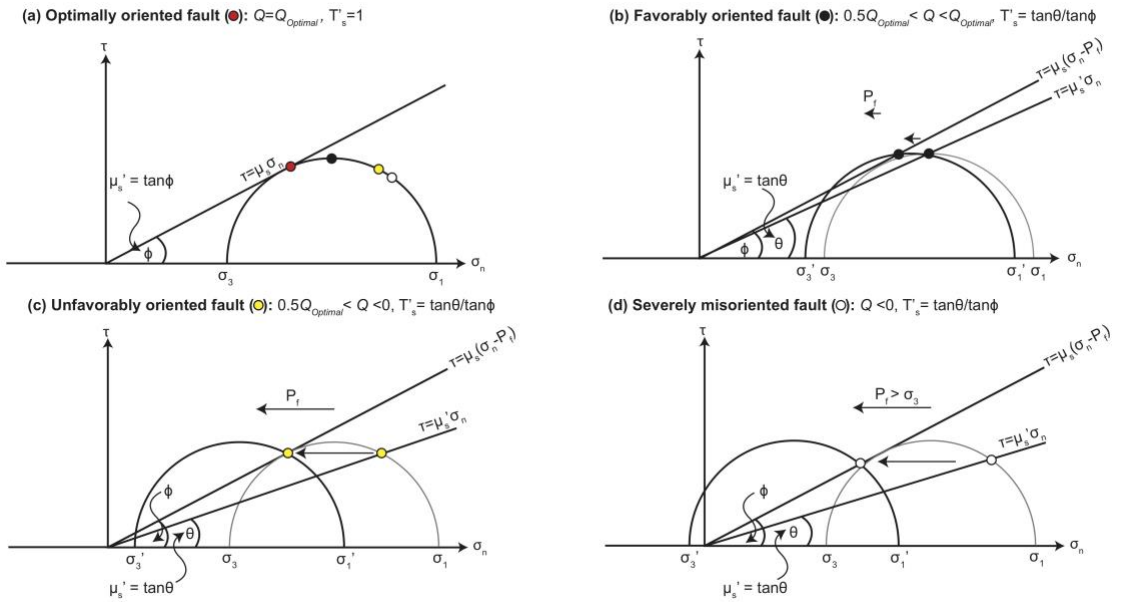

947
948 Figure 6: Illustration in Mohr Space of different concepts for analyzing fault reactivation. (a)
949 The stress ratio (Q=σ_3/σ_1), normalized slip tendency (T'_s), and effective coefficient of friction
950 (μ_s') acting on an optimally oriented cohesionless fault. In this case, Q= $Q_{Optimal}$, T'_s = 1, μ_s'
951 is the same as the frictional strength of an optimally oriented fault (μ_s=tanϕ), and no fluid
952 pressure (P_f) is required for reactivation. In addition, the orientation of three hypothetical
953 faults is also depicted. The Q, T'_s, μ_s', and P_f required for reactivation of these (b) favorably
954 oriented, (c) unfavorably oriented, and (d) severely misoriented fault is then also shown. For
955 clarity, this example is for a 2-D reactivation analysis when the fault plane contains σ_2.
956 However, the principles are the same for a 3-D analysis.

957

958 Figure 7

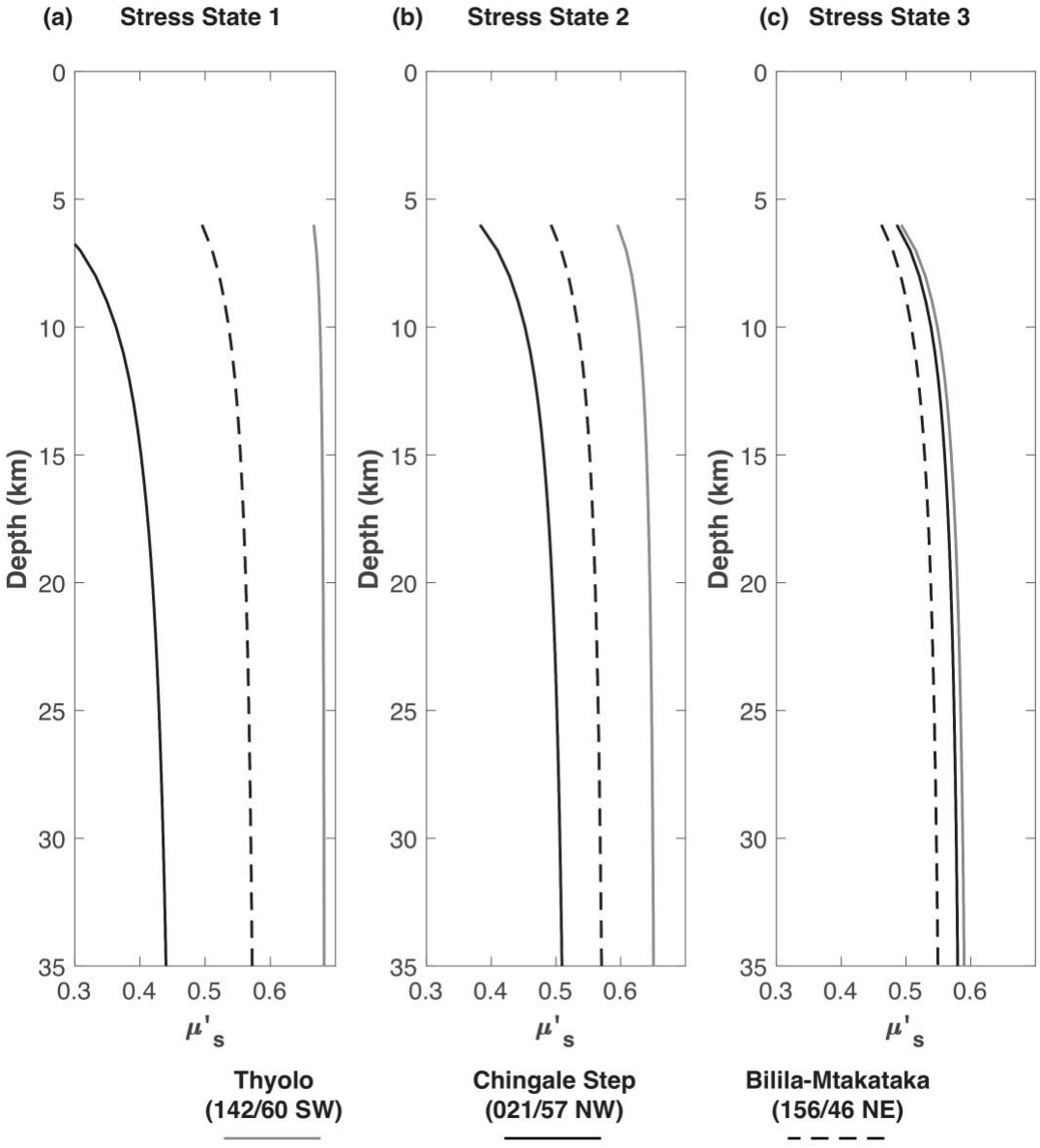

959

960 Figure 7: The effective coefficient of friction (μ_s') required to reactivate the Thyolo, Chingale
961 Step, and Bilila-Mtakataka fault in (a-c) Stress States 1-3 between depths 6-35 km. Analysis
962 for cohesive faults (c=40 MPa), with no fluid pressure, intact rock strength μ_i=0.7, and stress
963 shape ratio Φ=0.43, and density model in Table S2. For equivalent figures for cohesionless
964 faults, see Figure S9.

965

966 Figure 8
967

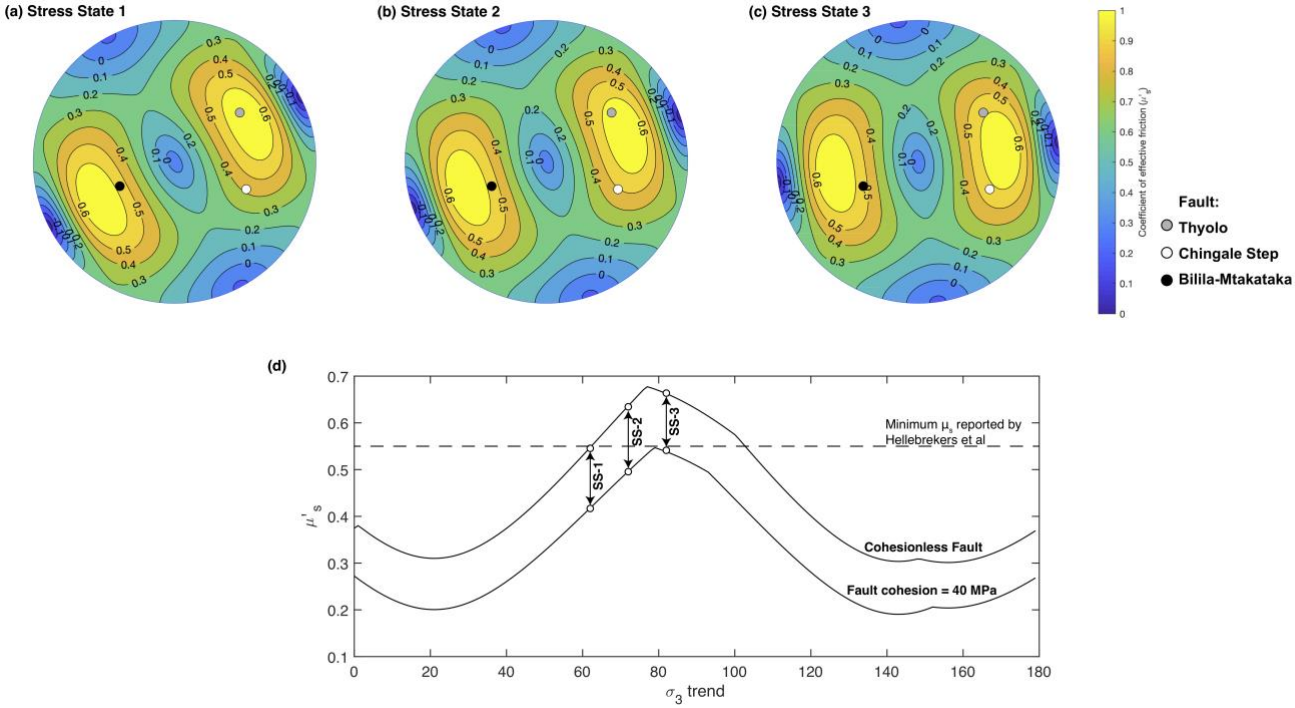

968
969 Figure 8: (a-c) Stereoplots contoured by the effective coefficient of friction (μ'_s) required to
970 reactivate a cohesive fault (c=40 MPa) of any orientation in Stress States 1-3. Poles to the
971 fault orientations analyzed here are also shown. Equivalent plots for a cohesionless fault are
972 shown in Figure S7. (d) The maximum μ'_s in which all three faults analyzed here reactivate
973 as a function of σ_3 trend. SS-1, SS-2, and SS-3 mark points where Stress States 1-3 plot
974 respectively. Horizontal line represents lowest μ_s of basement rocks in Malawi reported by
975 Hellebrekers et al. [2019]. All results for a depth of 20-km, assuming the density model in
976 Table S2, and that σ_2 and σ_3 equal S_{Hmax} and S_{hmin} respectively. For all plots the intact rock
977 strength μ_i=0.7, stress shape ratio Φ=0.43, and there is no fluid pressure. Stereoplots
978 constructed using Cardozo in Allmendinger et al., [2011].

979

980 Figure 9

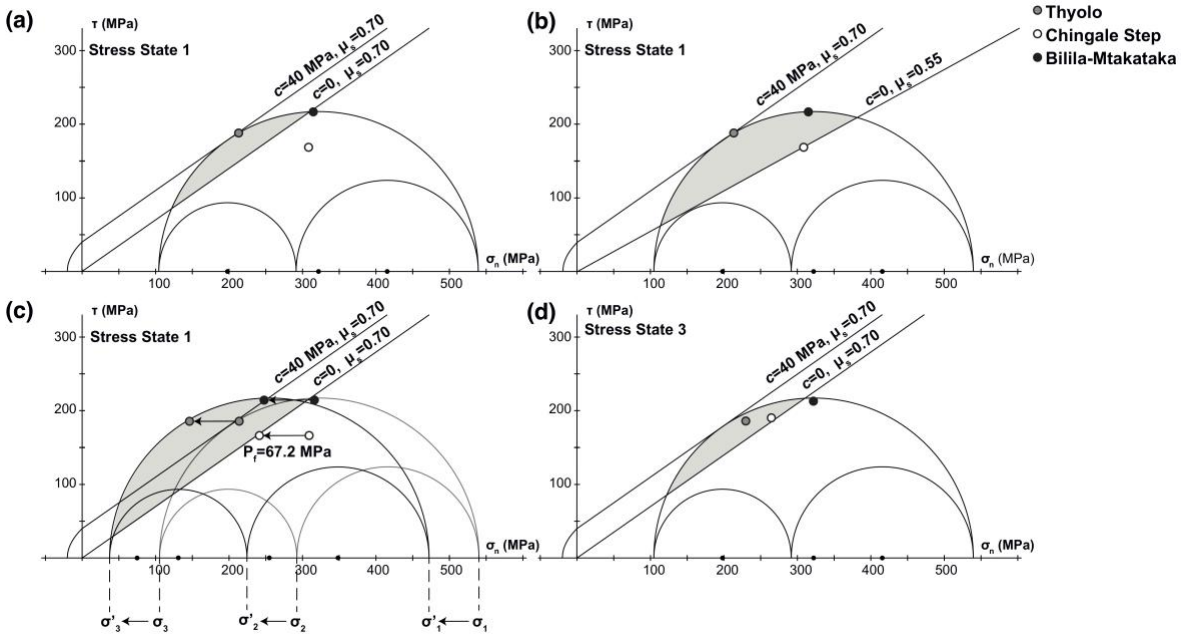

981

982 Figure 9: Three-dimensional Mohr Circle analysis for fault reactivation in southern Malawi at
983 20-km depth. Shaded region in each plot depicts range of orientations where a cohesionless
984 fault will reactivate. (a) Orientation of Thyolo, Chingale Step and Bilila-Mtakataka Fault in
985 Stress States 1. Given the failure criterions assumed here, only the Thyolo and Bilila-
986 Mtakataka fault will reactivate. Reactivation of the Chingale Step fault instead requires that
987 (b) μ_s'=0.55 or that (c) P_f' = 67.2 MPa (equivalent to λ_v'=0.12). (d) Same as (a) but for Stress
988 State 3. The Thyolo and Chingale Step faults will reactivate in this stress state and
989 reactivation of Bilila-Mtakataka requires a slight reduction in μ_s' to 0.66 (Table 3). Analysis
990 assumes Φ=0.43 and density model in Table S2.

991

992 Figure 10

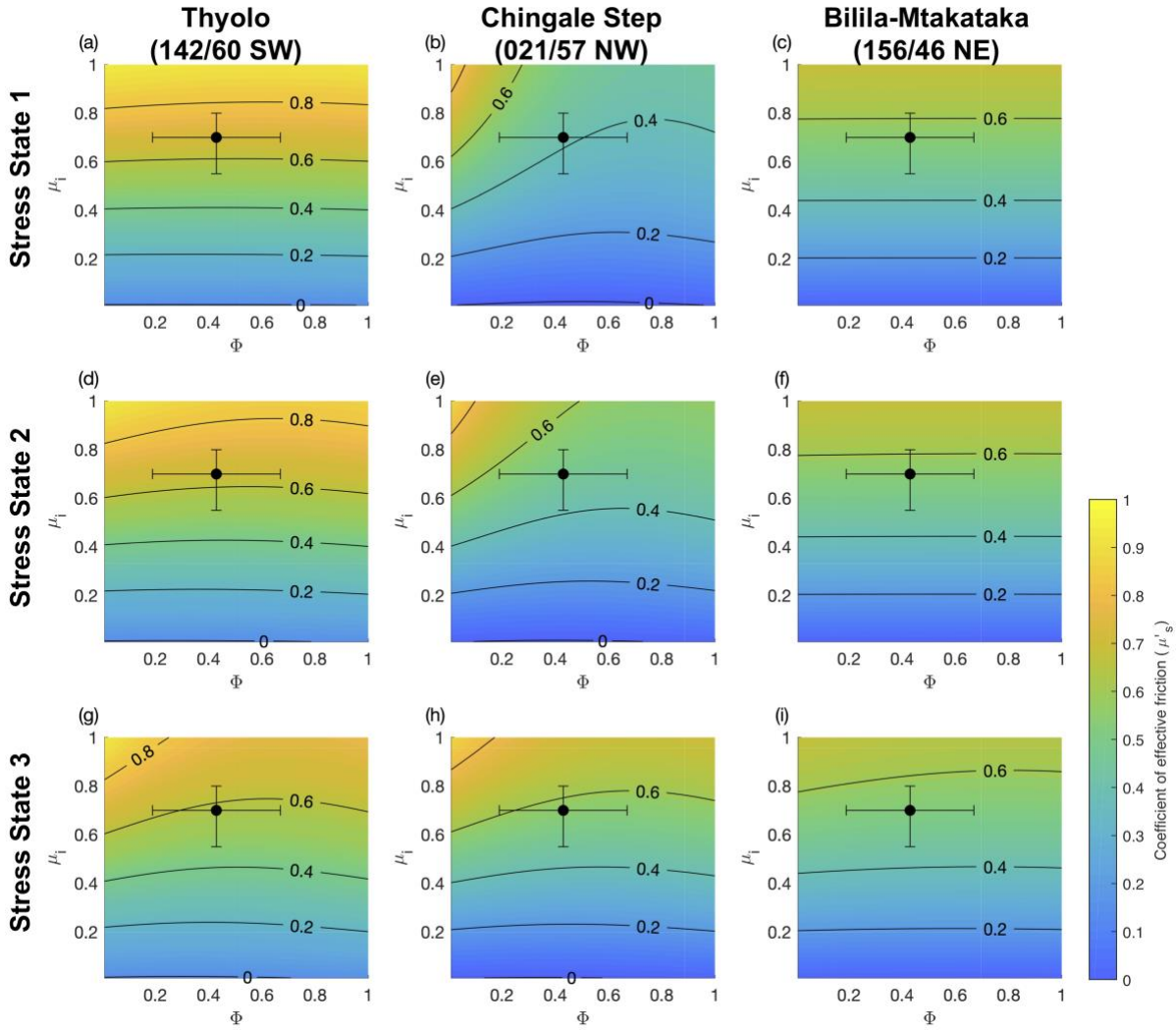

993
994 Figure 10: Contour plots for effective coefficient of friction (μ_s') needed for reactivation of a
995 cohesive fault (c=40 MPa) in intact rock frictional strength-stress shape ratio (μ_i-Φ) space for
996 the given fault orientations and Stress States 1-3 at 20 km depth. Black circle represents point
997 where Φ=0.43 and μ_i=0.70, as used in Figure 7, with error bars representing range of μ_i
998 reported by *Hellebrekers et al.*, [2019; μ_i=0.55-0.80], and 1 standard deviation uncertainty in
999 Φ (0.43 ± 0.24). For similar analysis for cohesionless fault, see Figure S10.

1000
1001

1002 **List of tables**

1003 Table 1

Event	Date (yyyy/mm/dd)	M_w	Longitude	Latitude	Depth (km)	Catalog	Strike	Dip	Rake	Rejected	Misfit (°)	Notes
a	1954/01/17	6.7	36.00	-16.50	20	DB2010	197	68	164	Y		
b	1966/05/06	5.1	34.60	-15.70	17	DB2010	001	51	-56		38.4	
c	1978/01/08	4.9	34.45	-11.76	15	DB2010	158	45	-90		1.9	
d	1989/03/09	5.5	34.47	-13.68	31	C2011	340	56	-99	Y		Same as event 4 in DB2010
e	1989/03/10	6.1	34.49	-13.71	32	C2011	336	56	-92		5.9	Same as event 5 in DB2010
f	1989/09/05	5.4	34.46	-11.80	19.8	DB2010	063	52	149	Y		
g	1994/11/16	4.5	33.51	-9.42	7	C2011	301	64	-11	Y		Focal mechanism from gCMT
h	1995/07/22	4.9	34.84	-13.98	33	C2011	158	42	-105		19.1	
i	1995/09/30	4.7	34.40	-13.82	30	C2011	321	54	-75		2.6	
j	1996/08/30	4.5	34.10	-15.40	10	DB2010	154	71	-109		2.6	
k	1998/08/24	4.7	34.89	-13.77	44	C2011	163	37	-95		3.8	Same as event 7 in DB2010
l	1999/09/01	4.7	34.20	-10.10	10	DB2010	022	81	-144	Y		
m	2000/01/04	4.8	36.10	-16.10	25	DB2010	352	66	-70		13.8	
n	2002/08/31	5.0	34.23	-9.84	20	C2011	355	53	-126		29.7	Same as event 9 in DB2010
o	2004/03/14	4.8	34.35	-10.08	29	DB2010	017	52	-117		14.0	

p	2004/08/21	4.7	34.44	-10.60	12	DB2010	084	75	-17		6.1
q	2009/12/06	5.7	33.85	-10.13	6	C2011	168	38	-91		4.8
r	2009/12/09	5.8	33.88	-9.95	6	C2011	167	41	-70		31.1
s	2009/12/12	5.5	33.91	-9.94	4	C2011	169	37	-95		0.8
t	2009/12/19	5.9	33.82	-10.11	5	C2011	149	46	-77		2.8
u	2018/03/08	5.5	35.427	-16.760	17	USGS	316	45	-94	Y	

Table 1: Compilation of earthquake focal mechanisms for the Malawi Rift. Catalogue codes are: (1) DB2010, *Delvaux and Barth*, [2010] and references therein, (2) C2011, *Craig et al.*, (2011) and references therein, (3) USGS, *U.S. Department of the Interior U.S. Geological Survey*, [2018]. Focal mechanisms from C2011 are from waveform modelling unless otherwise stated. The reported nodal plane is the one favored by the stress inversion (i.e., the plane with the smallest misfist, the magnitude of which is also reported). We also indicate which mechanisms were filtered during the stress inversion. Map of focal mechanisms is given in Figure 1. gCMT; Global Centroid Moment Tensor Project.

Table 2

Fault	Sample	Quartz	Albite	Biotite	Muscovite	Actinolite	Kaolinite	Montmorillonite	Dolomite	Prehnite	Calcite
Thyolo	Country rock	43	40			14	3				
	Fault rock	81					8	5		6	
Chingale Step	Country rock	30	30	37			3				
	Fault rock	4						2	1		93
Bilila-Mtakataka	Country rock	11	52		8	26	3				
	Fault rock	74	16								10

Table 2: Quantitative XRD (as weight %) of samples collected from fault zones in the Malawi Rift. Results are normalized to 100% and so do not include estimates of unidentified or amorphous material. XRD diffractograms are given in Figure S6.

Table 3

Stress State	Fault	Stress ratio (Q)				Slip tendency (T_s)	Normalized slip tendency (T'_s)	Effective coefficient of friction (μ_s')	
		c=0	Class	c=40-MPa	Class			c=0	c=40 MPa
1: σ_3 = 06/242	Thyolo	0.24	F	0.16	F	0.65	0.92	0.87	0.68
	Chingale Step	0.02	U	-0.08	S	0.43	0.62	0.55	0.42
	Bilila-Mtakataka	0.24	F	0.16	F	0.65	0.93	0.69	0.56
2: σ_3 = 10/072	Thyolo	0.24	F	0.16	F	0.62	0.88	0.81	0.64
	Chingale Step	0.19	F	0.11	U	0.56	0.81	0.65	0.50
	Bilila-Mtakataka	0.01	U	-0.09	S	0.45	0.65	0.69	0.56
3: σ_3 = 00/082	Thyolo	0.22	F	0.13	F	0.60	0.86	0.74	0.58
	Chingale Step	0.21	F	0.12	F	0.59	0.85	0.72	0.57
	Bilila-Mtakataka	0.17	F	0.08	U	0.56	0.80	0.66	0.54

Table 3: Results of fault reactivation analysis in terms of the stress ratio (Q), slip tendency (T_s), normalized slip tendency (T'_s), and effective frictional strength (μ_s') needed to reactivate each fault in Stress States 1-3. F-favorably oriented fault (Q>0.5$Q_{Optimal}$); U-unfavorably oriented fault (0.5$Q_{Optimal}$<Q<0), S-severely misoriented fault [Q<0, Figure 6; *Leclère & Fabbri*, 2013; *Sibson*, 1985]. T_s, T'_s, and Q where c=0 pertain to any depth. Q where c=40 MPa and μ_s' are for a depth of 20-km, and assume a fault surrounded by intact rock where μ_i=0.7. See Figures 7 and S9 for how these values vary with depth. All results to 2 decimal places.